http://tandfonline.com/ixen
ISSN: 0049-8254 (print), 1366-5928 (electronic)

Xenobiotica

Xenobiotica, 2016; 46(4): 289–295
 DOI: 10.3109/00498254.2015.1074301

Taylor & Francis
Taylor & Francis Group

RESEARCH ARTICLE

Raloxifene glucuronidation in liver and intestinal microsomes of humans and monkeys: contribution of UGT1A1, UGT1A8 and UGT1A9

Naoki Kishi[1], Akane Takasuka[1], Yuki Kokawa[1], Takashi Isobe[2], Maho Taguchi[3], Masato Shigeyama[3], Mikio Murata[3], Manabu Suno[1], and Nobumitsu Hanioka[2]

[1]*Faculty of Pharmaceutical Sciences, Okayama University, Okayama, Japan,* [2]*Department of Biochemical Toxicology, and* [3]*Department of Clinical Pharmacy, Yokohama University of Pharmacy, Yokohama, Japan*

Abstract

1. Raloxifene is an antiestrogen that has been marketed for the treatment of osteoporosis, and is metabolized into 6- and 4′-glucuronides by UDP-glucuronosyltransferase (UGT) enzymes. In this study, the *in vitro* glucuronidation of raloxifene in humans and monkeys was examined using liver and intestinal microsomes and recombinant UGT enzymes (UGT1A1, UGT1A8 and UGT1A9).
2. Although the K_m and CL_{int} values for the 6-glucuronidation of liver and intestinal microsomes were similar between humans and monkeys, and species differences in V_{max} values (liver microsomes, humans > monkeys; intestinal microsomes, humans < monkeys) were observed, no significant differences were noted in the K_m or S_{50}, V_{max} and CL_{int} or CL_{max} values for the 4′-glucuronidation of liver and intestinal microsomes between humans and monkeys.
3. The activities of 6-glucuronidation in recombinant UGT enzymes were UGT1A1 > UGT1A8 > UGT1A9 for humans, and UGT1A8 > UGT1A1 > UGT1A9 for monkeys. The activities of 4′-glucuronidation were UGT1A8 > UGT1A1 > UGT1A9 in humans and monkeys.
4. These results demonstrated that the profiles for the hepatic and intestinal glucuronidation of raloxifene by microsomes were moderately different between humans and monkeys.

Keywords

Glucuronidation, humans, intestinal microsomes, liver microsomes, monkeys, raloxifene

History

Received 20 June 2015
Revised 14 July 2015
Accepted 15 July 2015
Published online 6 August 2015

Introduction

Raloxifene is a second-generation selective estrogen receptor modulator that has been approved for the prevention and treatment of osteoporosis in post-menopausal women (D'Amelio & Isaia, 2013; Hansdóttir, 2008). It also functions as an estrogen agonist in breast and uterine tissues, and is currently prescribed for the chemoprevention of breast cancer (Gizzo et al., 2013; Moen & Keating, 2008). Raloxifene is rapidly absorbed after its oral administration in humans, and has been found to undergo extensive pre-systemic glucuronidation, resulting in only 2% bioavailability (Morello et al., 2003; Snyder et al., 2000). Furthermore, these clinical studies reported that the principal metabolic pathways of raloxifene were 6- and/or 4′-glucuronides formed by UDP-glucuronosyltransferase (UGT) enzymes (Figure 1).

Address for correspondence: Nobumitsu Hanioka, Department of Biochemical Toxicology, Yokohama University of Pharmacy, 601 Matano-cho, Totsuka-ku, Yokohama 245-0066, Japan. E-mail: nhanioka@hamayaku.ac.jp

Kemp et al. (2002) demonstrated that raloxifene glucuronidation was catalyzed by UGT1A1, UGT1A8, UGT1A9 and UGT1A10 in humans. Of these UGT isoforms, UGT1A8 and UGT1A10 were shown to be expressed in extrahepatic tissues such as the small intestine and colon, but not in the liver (Harbourt et al., 2012; Ohno & Nakajin, 2009; Tukey & Strassburg, 2000). The *in vitro* clearance (CL_{int}) values for the 4′-glucuronidation of intestinal microsomes were previously shown to be 3- to 10-fold higher than those of liver microsomes in humans (Cubitt et al., 2009; Dalvie et al., 2008; Jeong et al., 2005; Kemp et al., 2002). These *in vitro* findings suggest that raloxifene is mainly glucuronidated in the intestine, leading to markedly low bioavailability (Morello et al., 2003; Snyder et al., 2000).

Information on species differences in the *in vitro* glucuronidation of raloxifene in liver and intestinal microsomes is limited. Jeong et al. (2005) found that the total CL_{int} values of 6- and 4′-glucuronidation of human intestinal microsomes were 3- to 6-fold higher than those of rat intestinal microsomes, but were similar in liver microsomes. Kosaka et al. (2011) showed that the total CL_{int} values of the intestinal microsomes of humans, monkeys and dogs were 2- to 7-fold higher than those of liver microsomes in all species, with that of human intestinal microsomes being the highest.

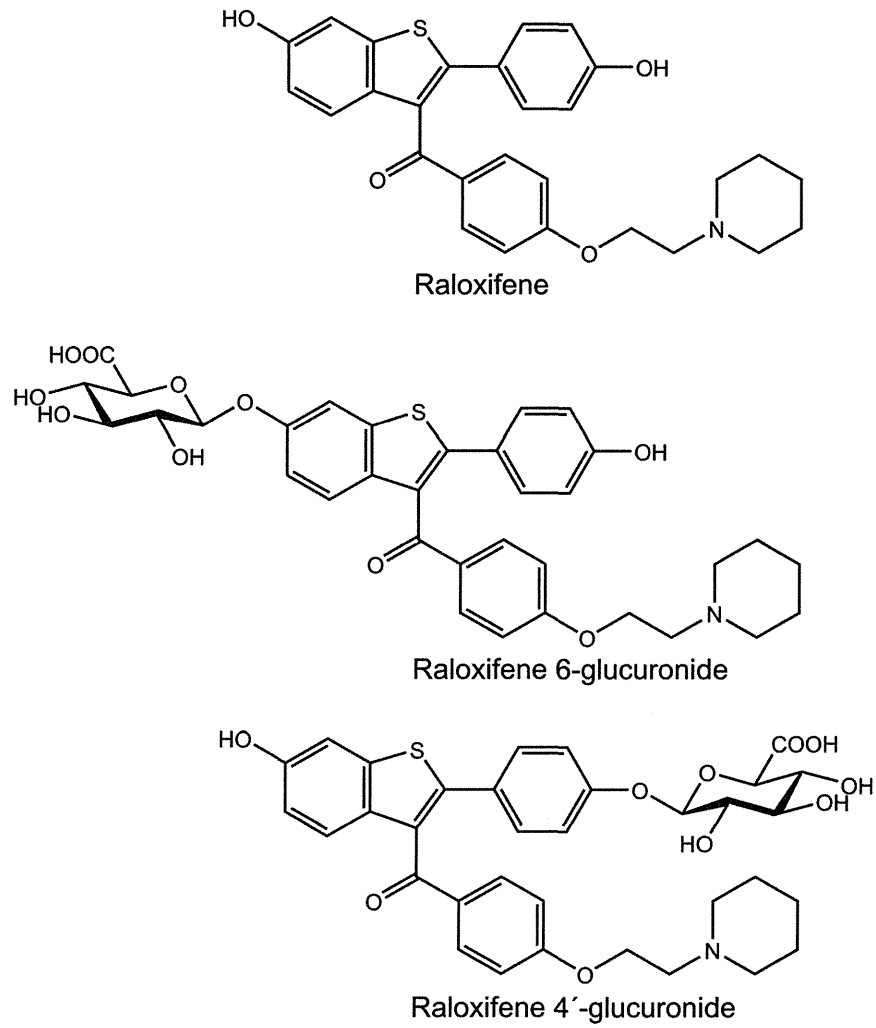

Figure 1. Chemical structures of raloxifene and its glucuronides.

Variations among species have been attributed to the tissue distribution, expression levels and functions of the UGT isoforms responsible for raloxifene glucuronidation in each species.

Many UGT isoforms have been suggested to be expressed in the hepatic and/or extrahepatic tissues of mammals including humans, monkeys and rodents (Mackenzie et al., 1997, 2005; Tukey & Strassburg, 2000). Furthermore, several UGT cDNAs of monkeys, rats, and mice have been cloned (http://www.flinders.edu.au/medicine/sites/clinical-pharmacology/ugt-homepage.cfm), and the functions of each UGT isoform coded by cDNA have been characterized (Kiang et al., 2005; Ritter, 2000). Monkeys are generally regarded as experimental animals that are similar to humans in studies on safety evaluation and biotransformation for the development of medicines. Although the cDNAs encoding the orthologs of several human UGT isoforms have been cloned in monkeys, the roles of each UGT isoform responsible for the glucuronidation of raloxifene in monkeys have not yet been reported.

The aim of this study was to investigate species differences in the hepatic and intestinal glucuronidation of raloxifene between humans and monkeys in an *in vitro* system. To achieve this, the glucuronidation activities of raloxifene in the liver and intestinal microsomes of humans and monkeys were determined, and the contributions of UGT1A1, UGT1A8, and UGT1A9 in each species toward raloxifene were estimated using recombinant enzymes.

Materials and methods

Materials

Raloxifene was purchased from LKT Laboratories (St. Paul, MN). Raloxifene 6- and 4′-glucuronides were from Toronto Research Chemicals (Toronto, ON, Canada); alamethicin was from Sigma-Aldrich (St. Louis, MO); UDP-glucuronic acid was from Nacalai Tesque (Kyoto, Japan); and pooled microsomes of human livers (race, Caucasian, Hispanic, and African American; age: 20–78 years old), human intestines (race, Caucasian and Hispanic; age: 18–55 years old), monkey livers (strain, cynomolgus; age: 3–8 years old) and monkey intestines (strain, cynomolgus; age: 5–7 years old) were from XenoTech (Lenexa, KS). Recombinant UGT enzymes (human, UGT1A1, UGT1A8 and UGT1A9; monkey, UGT1A1 and UGT1A9) were expressed using insect cells (Sf9 cells) as described previously (Hanioka et al., 2010; Kokawa et al., 2013; Yamamoto et al., 2014). Recombinant monkey UGT1A8 was expressed in the same manner as human UGT1A8. Monkey UGT1A8 cDNA was cloned from the total RNA of a cynomolgus monkey colon (Biochain Institute, Newark, CA) using a nested PCR

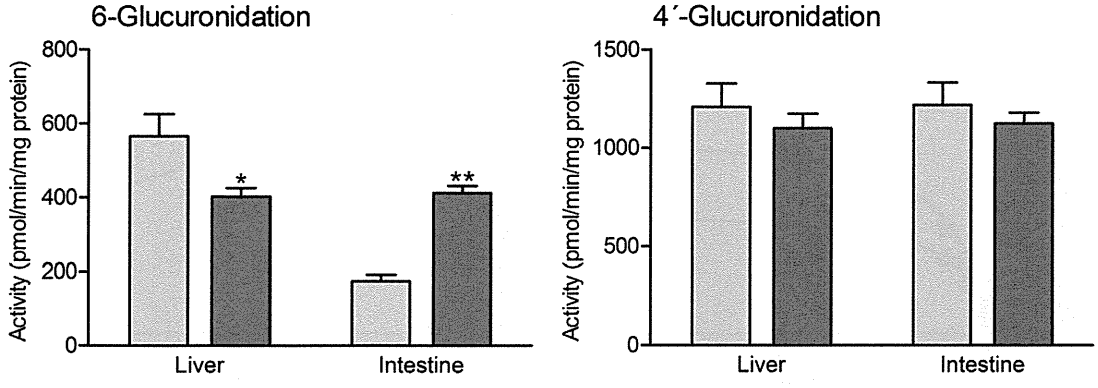

Figure 2. Raloxifene glucuronidation activities in liver and intestinal microsomes of humans and monkeys. The substrate concentration used was 10 μM. Each column represents the mean ± SD of three separate experiments. ▒, humans; ■, monkeys. Significantly different from human liver or intestinal microsomes (*$p<0.05$, **$p<0.01$).

method. Specific primer sets were designed on the basis of nucleotide sequences registered at GenBank (accession number, AF104337). All other chemicals and reagents used were of the highest quality commercially available.

Assay for raloxifene glucuronidation activity

Raloxifene glucuronidation activities were determined according to a previously described method with minor modifications (Kokawa et al., 2013). The incubation mixture contained raloxifene (0.2–100 μM), enzymes (50 μg protein/mL for liver and intestinal microsomes, 100 μg protein/mL for recombinant UGT enzymes), alamethicin (20 μg/mL), 10 mM $MgCl_2$ and 2 mM UDP-glucuronic acid in a final volume of 200 μL of 50 mM Tris-HCl buffer (pH 7.4). After a pre-incubation for 2 min at 37 °C, the reaction was initiated by the addition of UDP-glucuronic acid. Samples were incubated for 10 min at 37 °C, and the reaction was terminated by the addition of 100 μL of acetonitrile. Raloxifene was dissolved in methanol/dimethyl sulfoxide (50:50, v/v), and the final concentration of the organic solvent (methanol and dimethyl sulfoxide) in the incubation mixture was 1% (v/v). Samples were centrifuged at 12 000 × *g* for 10 min at 4 °C. The supernatant was filtered with a polytetrafluoroethylene membrane filter (0.45 μm), and 20 μL of the filtrate was subjected to high-performance liquid chromatography with an Inertsil Ph column (4.6 mm i.d. ×150 mm; GL Sciences, Tokyo, Japan). The column was maintained at 40 °C. Raloxifene 6- and 4′-glucuronides were isocratically eluted with 20 mM KH_2PO_4 (pH 3.5)/acetonitrile/methanol (70:15:15, v/v/v) at a flow rate of 1.0 mL/min. UV detection was performed at 287 nm. Standard curve samples spiked with 6- and 4′-glucuronides (each 0–500 pmol/mL) were prepared in the same manner as incubation samples.

Data analysis

Kinetic parameters (K_m or S_{50}, and V_{max}), the Hill coefficient (n) and K_{si} for raloxifene glucuronidation were calculated by constructing velocity versus substrate concentration (V-[*S*]) plots using SigmaPlot version 8.02 software (Systat Software, San Jose, CA). The kinetic profile was estimated from the respective coefficient of determination and/or Akaike's information criterion values for the Michaelis–Menten, isoenzyme, substrate inhibition and Hill equations. *In vitro* clearance values were CL_{int} (V_{max}/K_m) or CL_{max} ($V_{max}/S_{50} \times (n-1)/(n(n-1)^{1/n})$. All values were expressed as the mean ± SD of three separate experiments. Statistical comparisons were made with an unpaired two-tailed Student's *t*-test, and differences were considered significant when $p<0.05$.

Results

Raloxifene glucuronidation activities in liver and intestinal microsomes

Raloxifene 6- and 4′-glucuronidation activities in the liver and intestinal microsomes of humans and monkeys were determined at a substrate concentration of 10 μM (Figure 2). The activities of 6- and 4′-glucuronidation in humans were 566 and 1210 pmol/min/mg protein for liver microsomes, and 174 and 1220 pmol/min/mg protein for intestinal microsomes, respectively. Regarding 6-glucuronidation in monkeys, the activity in liver microsomes was 70% of that in human liver microsomes, whereas the activity in intestinal microsomes was 2.4-fold higher than that in human intestinal microsomes. The activities of 4′-glucuronidation in monkey liver and intestinal microsomes were similar to those in the respective microsomes of humans.

Kinetics for raloxifene glucuronidation by liver microsomes

Kinetic analyses of raloxifene 6- and 4′-glucuronidation by the liver microsomes of humans and monkeys were performed to obtain more detailed information. The plots (V-[*S*] and V-V/[*S*] plots) and parameters of the kinetics tested are shown in Figure 3 and Table 1, respectively. The kinetics for 6-glucuronidation by human and monkey liver microsomes followed the Michaelis–Menten model. The K_m, V_{max} and CL_{int} values of human liver microsomes were 7.90 μM, 1090 pmol/min/mg protein and 137 μL/min/mg protein, respectively. The K_m, V_{max} and CL_{int} values of monkey liver microsomes were 84, 61 and 73% of those of human liver microsomes, respectively, and significant differences were observed in V_{max} and CL_{int} values between human and monkey liver microsomes. The kinetics for 4′-glucuronidation by human and monkey liver microsomes exhibited a substrate inhibition model. The K_m, V_{max}, CL_{int} and K_{si} values of

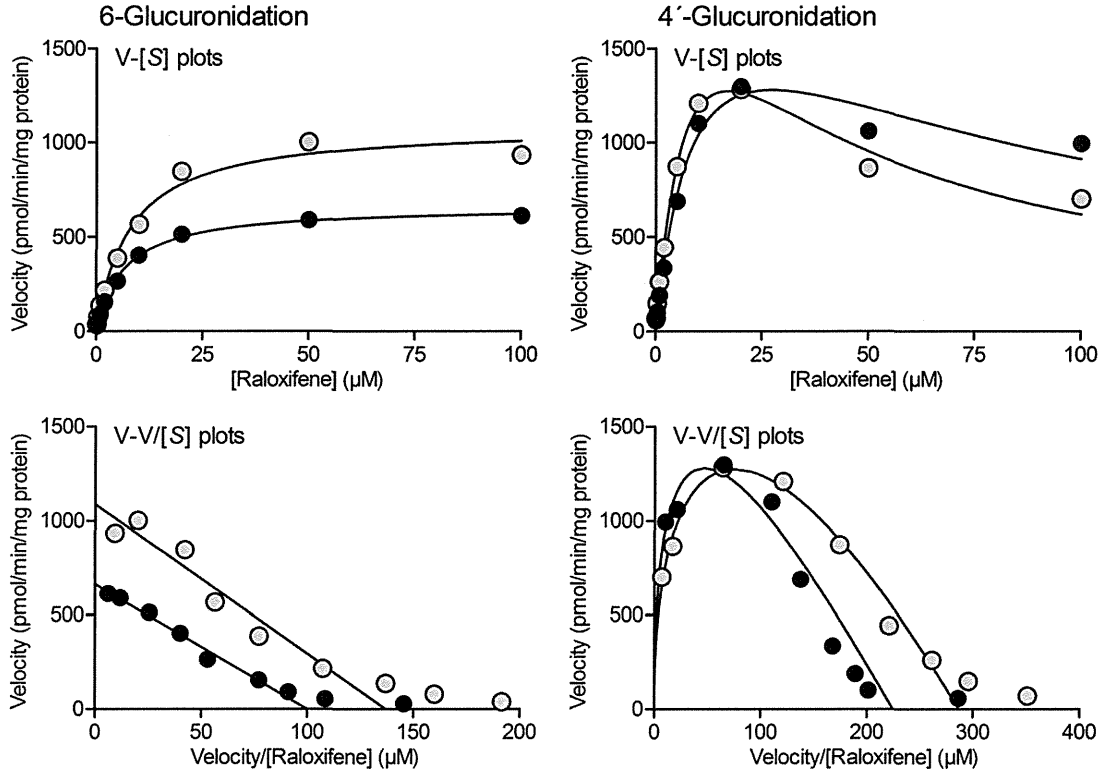

Figure 3. Kinetics of raloxifene glucuronidation by human and monkey liver microsomes. Substrate concentrations were 0.2–100 μM. Each point represents the mean of three separate experiments. ○, humans; ●, monkeys.

Table 1. Kinetic parameters for raloxifene glucuronidation by human and monkey liver microsomes.

	K_m (μM)	V_{max} (pmol/min/mg protein)	CL_{int} (μL/min/mg protein)	K_{si} (μM)	Model
6-Glucuronidation					
Human liver microsomes	7.90 ± 0.58	1090 ± 170	137 ± 16		Michaelis–Menten
Monkey liver microsomes	6.66 ± 0.71	663 ± 31*	100 ± 11*		Michaelis–Menten
4′-Glucuronidation					
Human liver microsomes	9.66 ± 1.67	2720 ± 240	286 ± 47	30.4 ± 5.4	Substrate inhibition
Monkey liver microsomes	9.85 ± 1.29	2210 ± 230	225 ± 16	76.9 ± 12.1**	Substrate inhibition

Each value represents the mean ± SD of three separate experiments. Significantly different from human liver microsomes (*$p < 0.05$, **$p < 0.01$).

human liver microsomes were 9.66 μM, 2720 pmol/min/mg protein, 286 μL/min/mg protein and 30.4 μM, respectively. The K_m value of monkey liver microsomes was similar to that of human liver microsomes. The V_{max} and CL_{int} values of monkey liver microsomes were 81 and 79% of those of human liver microsomes, respectively; however, no significant differences were observed in any parameters. The K_{si} value of monkey liver microsomes was significantly higher (2.5-fold) than that of human liver microsomes.

Kinetics for raloxifene glucuronidation by intestinal microsomes

The kinetics for raloxifene 6- and 4′-glucuronidation by the intestinal microsomes of humans and monkeys were then analyzed. The plots (V-[S] and V-V/[S] plots) and parameters of the kinetics tested are shown in Figure 4 and Table 2, respectively. The kinetics for 6-glucuronidation by human and monkey intestinal microsomes exhibited the Michaelis–Menten model. The K_m, V_{max} and CL_{int} values of human intestinal microsomes were 1.49 μM, 216 pmol/min/mg protein and 148 μL/min/mg protein, respectively. The K_m and V_{max} values of monkey intestinal microsomes were significantly higher (2- and 2.5-fold, respectively) than those of human intestinal microsomes. Therefore, the CL_{int} value of monkey intestinal microsomes was similar to that of human intestinal microsomes. The kinetics for 4′-glucuronidation by human and monkey intestinal microsomes fit the Hill model with n of approximately 1.5. The S_{50}, V_{max} and CL_{max} values of human intestinal microsomes were 0.741 μM, 1210 pmol/min/mg protein and 870 μL/min/mg protein, respectively. The S_{50}, V_{max} and CL_{max} values of monkey intestinal microsomes were similar to those of human intestinal microsomes.

Raloxifene glucuronidation activities in recombinant UGT enzymes

Raloxifene 6- and 4′-glucuronidation activities in the recombinant UGT1A1, UGT1A8 and UGT1A9 enzymes of humans and monkeys were determined at a substrate concentration of 10 μM (Figure 5). The activities of 6- and 4′-glucuronidation in human UGT enzymes were 154 and 74.4 pmol/min/mg

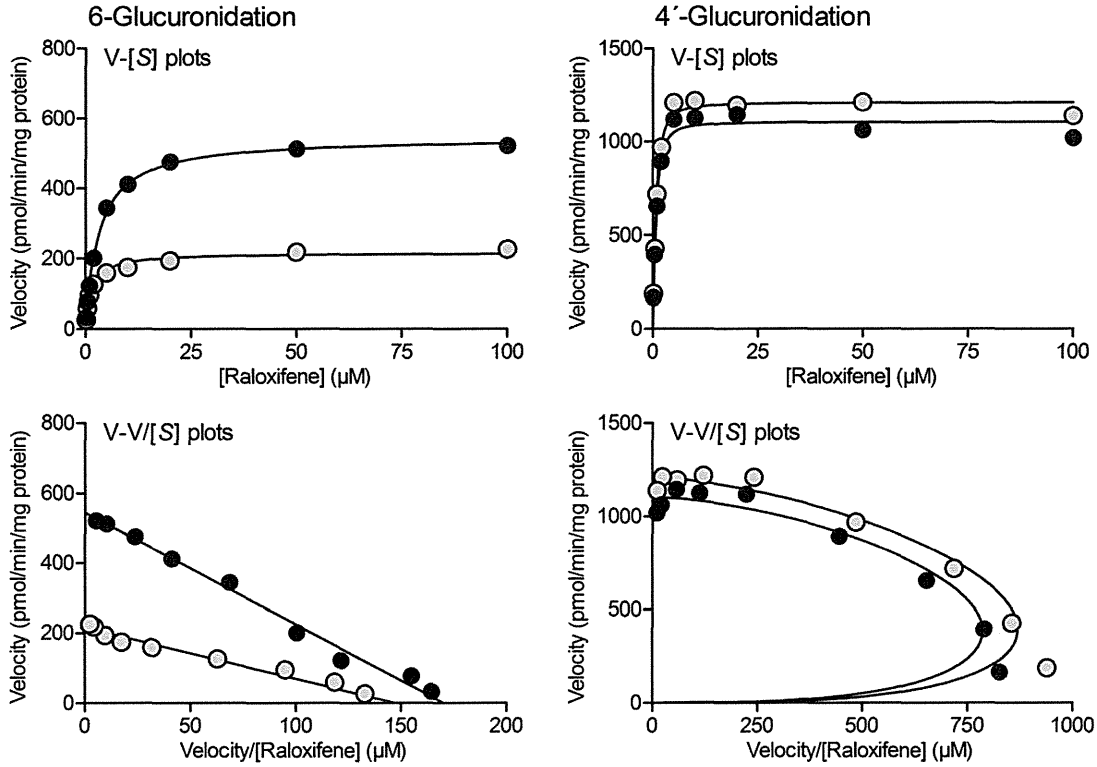

Figure 4. Kinetics of raloxifene glucuronidation by human and monkey intestinal microsomes. Substrate concentrations were 0.2–100 μM. Each point represents the mean of three separate experiments. ○, humans; ●, monkeys.

Table 2. Kinetic parameters for raloxifene glucuronidation by human and monkey intestinal microsomes.

	K_m or S_{50} (μM)	V_{max} (pmol/min/mg protein)	CL_{int} or CL_{max} (μL/min/mg protein)	n	Model
6-Glucuronidation					
Human intestinal microsomes	1.49 ± 0.20	216 ± 18	148 ± 31		Michaelis–Menten
Monkey intestinal microsomes	3.20 ± 0.11**	545 ± 21**	170 ± 12		Michaelis–Menten
4′-Glucuronidation					
Human intestinal microsomes	0.741 ± 0.009	1210 ± 120	870 ± 69	1.48 ± 0.05	Hill
Monkey intestinal microsomes	0.740 ± 0.035	1110 ± 110	788 ± 41	1.54 ± 0.13	Hill

Each value represents the mean ± SD of three separate experiments. Significantly different from human intestinal microsomes (**$p < 0.01$).

protein for UGT1A1, 80.3 and 174 pmol/min/mg protein for UGT1A8 and 16.7 and 27.7 pmol/min/mg protein for UGT1A9, respectively. The activities of 6- and 4′-glucuronidation in monkey UGT1A1 were similar to those in human UGT1A1. The activities of monkey UGT1A8 were significantly higher (2.7-fold) in 6-glucuronidation, and significantly lower (42%) in 4′-glucuronidation than those of human UGT1A8. Regarding monkey UGT1A9, 6-glucuronidation activity was 16% that in human UGT1A9, whereas 4′-glucuronidation activity was not detectable.

Discussion

Raloxifene is currently used for the prevention and treatment of osteoporosis in post-menopausal women (D'Amelio & Isaia, 2013; Hansdóttir, 2008). It undergoes extensive pre-systemic glucuronidation, with only 2% reaching the systemic circulation (Morello et al., 2003; Snyder et al., 2000). Previous studies suggested that raloxifene glucuronidation was catalyzed by UGT1A1, UGT1A8, UGT1A9 and UGT1A10 in humans, and that UGT1A8 expressed in extrahepatic tissues played an important clinical role in the metabolism of raloxifene (Jeong et al., 2005; Kemp et al., 2002; Mizuma, 2009). Monkeys are commonly used as animal models for the development of medicines and characterization of the pharmacokinetics and toxicological properties of novel compounds. In this study, the species difference in the *in vitro* glucuronidation of raloxifene between humans and monkeys was determined using liver and intestinal microsomes and recombinant UGT enzymes.

In order to obtain basic information on the hepatic and intestinal glucuronidation of raloxifene in humans and monkeys, raloxifene 6- and 4′-glucuronidation activities in the liver and intestinal microsomes of humans and monkeys were initially determined at a single substrate concentration. The activities of 4′-glucuronidation in liver and intestinal microsomes were higher than those of 6-glucuronidation in humans and monkeys. Regioselective glucuronidation of raloxifene in human liver and intestinal microsomes was consistent with previous findings (Kemp et al., 2002;

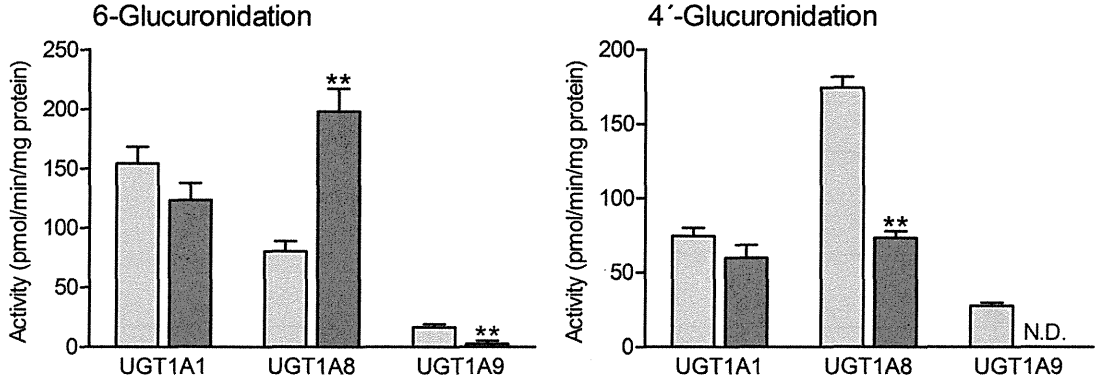

Figure 5. Raloxifene glucuronidation activities in recombinant UGT enzymes of humans and monkeys. The substrate concentration used was 10 μM. Each column represents the mean ± SD of three separate experiments. ○, humans; ●, monkeys. Significantly different from human recombinant UGT enzymes (**$p < 0.01$).

Lušin et al., 2011). Although no significant difference was observed in 4′-glucuronidation activities between humans and monkeys in any liver and intestinal microsomes, species differences in 6-glucuronidation activities in microsomes showed the opposite profile (liver microsomes, humans > monkeys; intestinal microsomes, humans < monkeys). These phenomena were attributed to the UGT isoforms involved in raloxifene glucuronidation and their expression levels in the liver and intestine were different between humans and monkeys.

Kinetic analyses of raloxifene glucuronidation by the liver and intestinal microsomes of humans and monkeys were subsequently performed at a broad range of substrate concentrations. Previous studies reported that the kinetics for 6-glucuronidation by human liver and intestinal microsomes fit the Michaelis–Menten model; however, K_m values (liver microsomes, 15–160 μM; intestinal microsomes, 4.9–58 μM) varied among studies (Jeong et al., 2005; Kemp et al., 2002; Lušin et al., 2011). The kinetics by human liver and intestinal microsomes in this study also followed the Michaelis–Menten model; K_m values were consistent with those reported by Jeong et al. (2005) in both microsomes.

The kinetics for 6-glucuronidation by the liver and intestinal microsomes of monkeys fit the Michaelis–Menten model, as observed in human liver and intestinal microsomes. The K_m values of monkey liver and intestinal microsomes were similar and 2-fold higher than those of human liver and intestinal microsomes, respectively. The V_{max} values of monkey liver and intestinal microsomes were significantly lower and higher than those of the respective microsomes of humans. The CL_{int} values of monkey liver and intestinal microsomes were similar to the respective microsomes of humans, although a significant difference was observed in human liver microsomes. On the other hand, the kinetics for 4′-glucuronidation followed the substrate inhibition model for liver microsomes and the Hill model for intestinal microsomes in humans and monkeys. In addition, the parameter values of kinetics by liver and intestinal microsomes were similar between humans and monkeys. These results obtained by kinetic analyses demonstrated that moderate species differences existed in the hepatic and intestinal glucuronidation of raloxifene between humans and monkeys at the 6-position only.

We also determined the activities of raloxifene glucuronidation in the recombinant UGT1A1, UGT1A8 and UGT1A9 enzymes of humans and monkeys at a single substrate concentration. These UGT isoforms have been reported to be responsible for raloxifene glucuronidation in humans (Kemp et al., 2002). The activities of 6- and 4′-glucuronidation in human and monkey UGT1A1 were similar. A species difference was observed in regioselective glucuronidation by UGT1A8 (6-glucuronidation, humans < monkeys; 4′-glucuronidation, humans > monkeys). Human UGT1A9 was capable of catalyzing 6- and 4′-glucuronidation; in contrast, monkey UGT1A9 had low activity in 6-glucuronidation only. Among the recombinant UGT enzymes examined, the activity of 6-glucuronidation was the highest in monkey UGT1A8, while that of 4′-glucuronidation was the highest in human UGT1A8. Thus, this phenomenon was attributed to differences in the enzymatic properties of UGT1A8 between humans and monkeys, and UGT1A8 was reconfirmed to be a predominant enzyme for raloxifene glucuronidation in mammals. In addition, it was suggested that the contribution of UGT1A9 to raloxifene glucuronidation is less than that of UGT1A1 and UGT1A8 in both humans and monkeys.

The mRNA and protein of human UGT1A8 were previously found to be expressed in the small intestine and colon, but not in the liver (Harbourt et al., 2012; Ohno & Nakajin, 2009). Monkey UGT1A8 mRNA has been reported to be not only largely expressed in the large and small intestines, but also in the liver; however, its expression level was less than 0.5% in the large and small intestines (Nishimura et al., 2009). Kemp et al. (2002) showed that human UGT1A1 predominantly glucuronidated the 6-position of raloxifene. The expression levels of UGT1A1 mRNA in the liver and intestines (small intestine and colon or large intestine) were previously found to be approximately 3:2 for humans and 2:3 for monkeys, respectively (Ohno & Nakajin, 2009; Nishimura et al., 2009). The reverse profile of UGT1A1 expression may reflect the V_{max} values for raloxifene 6-glucuronidation activities by liver and intestinal microsomes in this study.

It has been suggested that exon 1 of UGT1As code the domain for binding of the substrate, while exons 2–5 code the domain for binding of UDP-glucuronic acid, and that the presence of different possible substrate-binding domains conferred large substrate specificity to UGT1A enzymes (Guillemette et al., 2010; Kiang et al., 2005; Ritter, 2000; Tukey & Strassburg, 2000). The amino acid homologies between human and monkey UGT1As in full length, exon 1 and common exons were 95.3 and 94.1% for UGT1A1, 94.7 and 91.1% for UGT1A8, 93.2 and 90.2% for UGT1A9 and 96.7%, respectively. Thus, the homologies between human and monkey UGT1As in exon 1 were low compared with exons 2–5. We previously reported that the enzymatic properties of human and monkey UGT1A1s are very similar, whereas the enzymatic properties of UGT1A9 are considerably different between humans and monkeys (Hanioka et al., 2010; Yamamoto et al., 2014), although there is no data for the species difference in UGT1A8 enzyme. The opposite profile for raloxifene 6-glucuronidation activities in liver and intestinal microsomes between humans and monkeys can be at least considered to be due to the structure in N-terminal domain and function of UGT1A9 and/or UGT1A8 enzymes. Further *in vitro* studies using chimeric and point mutated enzymes of human and monkey UGT1As are required to demonstrate the molecular mechanism of species differences in raloxifene glucuronidation.

Conclusions

The *in vitro* glucuronidation of raloxifene in humans and monkeys was examined using liver and intestinal microsomes and recombinant UGT enzymes. The activities of 6-glucuronidation in microsomes were humans > monkeys for liver microsomes, and humans < monkeys for intestinal microsomes. No significant differences were observed in the activities of 4′-glucuronidation activities between humans and monkeys in any liver and intestinal microsomes. The activities of 6-glucuronidation in recombinant UGT enzymes were UGT1A1 > UGT1A8 > UGT1A9 for humans, and UGT1A8 > UGT1A1 > UGT1A9 for monkeys. The activities of 4′-glucuronidation were UGT1A8 > UGT1A1 > UGT1A9 in humans and monkeys. These results demonstrated that the profiles of raloxifene glucuronidation in liver and intestinal microsomes were moderately different between humans and monkeys.

Declaration of interest

The authors have no duality of interest to declare. This work was supported in part by a Grant-in-Aid for Scientific Research (26281028) from the Japan Society for the Promotion of Science.

References

Cubitt HE, Houston JB, Galetin A. (2009). Relative importance of intestinal and hepatic glucuronidation-impact on the prediction of drug clearance. Pharm Res 26:1073–83.

Dalvie D, Kang P, Zientek M, et al. (2008). Effect of intestinal glucuronidation in limiting hepatic exposure and bioactivation of raloxifene in humans and rats. Chem Res Toxicol 21:2260–71.

D'Amelio P, Isaia GC. (2013). The use of raloxifene in osteoporosis treatment. Expert Opin Pharmacother 14:949–56.

Gizzo S, Saccardi C, Patrelli TS, et al. (2013). Update on raloxifene: mechanism of action, clinical efficacy, adverse effects, and contra-indications. Obstet Gynecol Surv 68:467–81.

Guillemette C, Lévesque E, Harvey M, et al. (2010). UGT genomic diversity: beyond gene duplication. Drug Metab Rev 42:24–44.

Hanioka N, Tanabe N, Jinno H, et al. (2010). Functional characterization of human and cynomolgus monkey UDP-glucuronosyltransferase 1A1 enzymes. Life Sci 87:261–8.

Hansdóttir H. (2008). Raloxifene for older women: a review of the literature. Clin Interv Aging 3:45–50.

Harbourt DE, Fallon JK, Ito S, et al. (2012). Quantification of human uridine-diphosphate glucuronosyl transferase 1A isoforms in liver, intestine, and kidney using nanobore liquid chromatography-tandem mass spectrometry. Anal Chem 84:98–105.

Jeong EJ, Liu Y, Lin H, Hu M. (2005). Species- and disposition model-dependent metabolism of raloxifene in gut and liver: role of UGT1A10. Drug Metab Dispos 33:785–94.

Kemp DC, Fan PW, Stevens JC. (2002). Characterization of raloxifene glucuronidation *in vitro*: contribution of intestinal metabolism to presystemic clearance. Drug Metab Dispos 30:694–700.

Kiang TK, Ensom MH, Chang TK. (2005). UDP-glucuronosyltransferases and clinical drug-drug interactions. Pharmacol Ther 106: 97–132.

Kokawa Y, Kishi N, Jinno H, et al. (2013). Effect of UDP-glucuronosyltransferase 1A8 polymorphism on raloxifene glucuronidation. Eur J Pharm Sci 49:199–205.

Kosaka K, Sakai N, Endo Y, et al. (2011). Impact of intestinal glucuronidation on the pharmacokinetics of raloxifene. Drug Metab Dispos 39:1495–502.

Lušin TT, Trontelj J, Mrhar A. (2011). Raloxifene glucuronidation in human intestine, kidney, and liver microsomes and in human liver microsomes genotyped for the *UGT1A1*28* polymorphism. Drug Metab Dispos 39:2347–54.

Mackenzie PI, Owens IS, Burchell B, et al. (1997). The UDP glycosyltransferase gene superfamily: recommended nomenclature update based on evolutionary divergence. Pharmacogenetics 7: 255–69.

Mackenzie PI, Bock KW, Burchell B, et al. (2005). Nomenclature update for the mammalian UDP glycosyltransferase (UGT) gene superfamily. Pharmacogenet Genomics 15:677–85.

Mizuma T. (2009). Intestinal glucuronidation metabolism may have a greater impact on oral bioavailability than hepatic glucuronidation metabolism in humans: a study with raloxifene, substrate for UGT1A1, 1A8, 1A9, and 1A10. Int J Pharm 378:140–1.

Moen MD, Keating GM. (2008). Raloxifene: a review of its use in the prevention of invasive breast cancer. Drugs 68:2059–83.

Morello KC, Wurz GT, DeGregorio MW. (2003). Pharmacokinetics of selective estrogen receptor modulators. Clin Pharmacokinet 42: 361–72.

Nishimura M, Koeda A, Morikawa H, et al. (2009). Tissue-specific mRNA expression profiles of drug-metabolizing enzymes and transporters in the cynomolgus monkey. Drug Metab Pharmacokinet 24: 139–44.

Ohno S, Nakajin S. (2009). Determination of mRNA expression of human UDP-glucuronosyltransferases and application for localization in various human tissues by real-time reverse transcriptase-polymerase chain reaction. Drug Metab Dispos 37:32–40.

Ritter JK. (2000). Roles of glucuronidation and UDP-glucuronosyltransferases in xenobiotic bioactivation reactions. Chem Biol Interact 129:171–93.

Snyder KR, Sparano N, Malinowski JM. (2000). Raloxifene hydrochloride. Am J Health Syst Pharm 57:1669–75.

Tukey RH, Strassburg CP. (2000). Human UDP-glucuronosyltransferases: metabolism, expression, and disease. Annu Rev Pharmacol Toxicol 40:581–616.

Yamamoto K, Mukai M, Nagaoka K, et al. (2014). Functional characterization of cynomolgus monkey UDP-glucuronosyltransferase 1A9. Eur J Drug Metab Pharmacokinet 39:195–202.

Building and Environment 94 (2015) 504–515

Contents lists available at ScienceDirect

Building and Environment

journal homepage: www.elsevier.com/locate/buildenv

Investigation of flow pattern in upper human airway including oral and nasal inhalation by PIV and CFD

Nguyen Lu Phuong [a, *], Kazuhide Ito [b]

[a] Division of Environmental Management, Faculty of Environment, Ho Chi Minh City – University of Natural Resources and Environment, 236B Le Van Sy Street, Ward 1, Tan Binh District, Ho Chi Minh City, Viet Nam

[b] Interdisciplinary Graduate School of Engineering Science, Kyushu University, 6-1 Kasuga-koen, Kasuga, Fukuoka 816-8580, Japan

ARTICLE INFO

Article history:
Received 6 August 2015
Received in revised form
2 October 2015
Accepted 9 October 2015
Available online 23 October 2015

Keywords:
Computer simulated person
Human airway model
Idealized human airway model
Breathing modes
Computational fluid dynamics
Particle image velocimetry

ABSTRACT

Breathing is one of the most essential processes in the human body. The basic functions of breathing are to exchange gases (supplying oxygen from ambient air and removing carbon dioxide from the blood) and also to exchange heat and moisture through mucous surfaces of the airway. During an average lifetime, human beings experience significant exposure to indoor air and countless of contaminants/particles via inhalation. In this study, experimental and numerical results of flow fields in a realistic respiratory model were obtained. Flow patterns in a realistic replica model of the human respiratory tract were investigated with particle image velocimetry (PIV) under three constant breathing conditions; 7.5, 15 and 30 L/min. Computational fluid dynamics (CFD) analyses were conducted on turbulent models with boundary conditions corresponding to the experimental models. We used four RANS turbulence models to predict airflow in a realistic human airway model: two low Reynolds (Re) number-type k–ε turbulence models, RNG k–ε model, and the SST k–ω model. The CFD results were compared with PIV data and showed relatively good agreement in trachea region in all cases.

1. Practical implications

Various types of computer simulated persons (CSPs) have been developed for conducting indoor environmental analyses. Recently, a CSP with a respiratory tract from the nostril inlet to the bronchial tubes has been reported. To validate computational models of a respiratory tract, there are two types of measurements: *in vivo* and *in vitro*. Though early observations were mainly made *in vivo*, these measurements have many limitations due to the complicated structure and small size of nasal passages. PIV measurements of *in vitro* flow patterns in realistic replicas of the human respiratory tract provide an attractive alternative. They provide greater understanding of physical behaviors as well as contribute to the validation of numerical simulations.

2. Introduction

Asthma and chronic obstructive pulmonary disease (COPD) are chronic respiratory diseases estimated to affect 235 million and 64 million people worldwide, respectively [1]. A number of epidemiological studies have shown consistent associations between increases in acute exposure to particulate air pollution and increases in human morbidity and mortality [2,3]. When focusing on health problems related to the respiratory system, it is important to understand the pollutant mass transported in respiration. As stated previously, the human airway is the path for the exchange of gases between the lung and the ambient air. In addition, this organ also is the body's first line of defense against harmful agents from the ambient air. An investigation of airflow characteristics in the human respiratory tract will provide valuable information to enhance the understanding of the transportation of inhaled particles and/or gas-phase contaminants through respiration. Flow characteristics, flow patterns, and turbulence characteristics in the respiratory tract are various factors that will contribute to this understanding.

Respiratory exposure is a function not only of the respiratory tract from nostril to the lung, but also from the interaction of indoor air quality and breathing contaminant concentration. In general, non-uniform flows and contaminant concentration distributions are formed in indoor environment because of the heterogeneous distributions of heat and contaminant sources. To further the understanding and prediction of breathing contaminant

* Corresponding author.
E-mail addresses: nlphuong@hcmunre.edu.vn (N.L. Phuong), ito@kyudai.jp (K. Ito).

http://dx.doi.org/10.1016/j.buildenv.2015.10.002
0360-1323/

concentrations, various types of computer simulated persons (CSPs, numerical thermal mannequin, or virtual mannequin) have been developed and applied by researchers [4–10]. In early efforts, a CSP was coupled with a computational fluid dynamics (CFD) technique to predict thermal sensation analysis, e.g. prediction of skin surface temperature distribution on a human model using a thermo-regulation model.

Later, CFD analyses were used to examine the characteristics of a contaminated indoor air ventilation system in a simplified room on a realistic human model with inhalation and metabolic heat by metabolic activity [11]. CFD analyses using a low Reynolds number k–ε model were conducted to examine the inhalation region of a human body in a stagnant environment [12]. Research on the simulation of the microclimate around the human body including exposure concentration analyses has been well summarized [13].

More recent efforts have focused on the development of a CSP that integrates the detailed anatomy of the respiratory tract from nostril opening to bronchial tubes [14–19]. These CSPs with a respiratory tract model have strong potential to contribute to the respiratory exposure concentration analysis and the understanding of airborne exposure mechanism.

The microclimate CFD analyses around CSPs have been validated by various types of experimental results, but this is not true of CFD predictions in airways. As CFD models advance to have capabilities and applications in this anatomy, validation is extremely important and valuable.

To validate a simulation of the respiratory tract, there are two types of measurements: *in vivo* and *in vitro*. Though early observations were mainly made *in vivo*, these measurements have many limitations due to the complex anatomy and small size of nasal passages. The study of the human airway airflow *in vitro* has been pursued by a number of researchers. In the 1990s, the Particle Image Velocimetry (PIV) technique emerged from laboratory studies to be used in fundamental research applications, from aerodynamics to indoor air flow studies [20–22]. This PIV method has also been applied to measure velocity fields in physiological models of the upper human airway [23–25]. Hopkins et al. [26] used PIV to characterize flows in a transparent replica model of the nasal cavity. Doorly et al. [27] investigated flow fields in the nasal cavity using both flow visualization and PIV. Heenan et al. [28] used endoscopic PIV to measure the velocity fields of the sagittal plane of an idealized model of the human oropharynx during steady inspiration.

There are also numerous experimental studies that have been conducted in order to study the relationship between airway model characteristics and particle deposition efficiencies. Cheng et al. [29] measured deposition efficiencies under different flow rates in a replica cast of human oral-tracheobronchial airways made from an adult cadaver. They found most of the large particles (diameters greater than 30 μm) would be captured in the oral cavity. Experimental aerosol deposition data was obtained by Grgic et al. [30] on various realistic upper airway casts. The authors concluded that both flow rate and particle size have a significant effect on deposition efficiency. Experimental studies can provide detailed measures of velocity distributions but they come at the expense of significant facilities. Anthony et al. [31] reported detailed information on the velocity field and particle inhalation associated with two different adult mannequins using a Laser Doppler anemometer. Kim and Chung reported the detail flow pattern of a realistic nasal cavity model via PIV measurements [32,33]. Recently, Spence et al. documented PIV measurement results for 2D and 3D flow patterns in a realistic nasal cavity [34,35]. Absent from this list, however, are flow field measurements in a respiratory tract with complex geometries, especially for a bronchial pathway connected with a realistic upper airway. This paper will present results for such a study.

CFD has been used by many researchers to study airflows in the complex human airway. They include the study of the air flow field distribution [36], the distribution of temperature [37–39], particle transportation, and particle deposition in human airways [40,41]. While computational simulations might be more cost effective compared to experimental testing, they still have some uncertainties. The first uncertainty comes from the idealized geometries. These are considered the largest source of errors in numerical simulations [42]. The airflow is, of course, strongly affected by the airway geometries. Simplifying the physiological geometry for computational reasons may lead to invalid results. Another uncertainty is the capability of the numerical model to precisely reproduce the physical phenomena in the complicated three-dimensional airway. For these reasons, experimental data in human airways are still necessary to validate computational results.

While previous studies did employ sophisticated computational models, most of these models only contained a portion of the airway system. To our knowledge, until the current research described here, there has not yet been a human airway model that combined a physiologically accurate nasal cavity, oral cavity, larynx, pharynx, trachea and tracheal bifurcations. This limitation has prevented a comprehensive understanding of the airflow patterns through the entire human airway. The development of an integrated human airway model with all of the organs represents a valuable addition to our understanding.

In this study, we conducted an *in vitro* experiment and numerical prediction to investigate the flow distribution in the realistic geometry of a human airway. The *in vitro* experiment and numerical prediction models (*in silico*) were reproduced from CT data of an actual human airway, described below in more detail. Detailed measurements from the Particle Image Velocimetry (PIV) technique, as well as the numerical simulation through Computational Fluid Dynamics (CFD), are challenging in the understanding of respiratory system.

The results of flow patterns in a realistic respiratory tract model using the PIV technique, a 3-dimensional printer, and refraction control technique will be described. The PIV measurements represent *in vitro* data, which contribute to the development and validation process of numerical simulations.

3. Methodologies

3.1. Creation of the in vitro experiment model

Original respiratory tract data were obtained using a Toshiba 64 multi-detector row computed tomography (MDCT) scanner. The subject was a nonsmoking Asian male volunteer, 35 years old, with a body mass index (BMI) of approximately 21. The CT scans produced 785 slices of the respiratory tract. The images are stored as standard Digital Imaging and Communications in Medicine (DICOM) data, a format commonly used for the transfer and storage of medical images. Fig. 1 shows the combined CT images of the human upper airway.

The original set of CT images is converted into a file format compatible with Mimics® (Materialise NV). This is a 3D imaging software that generates and modifies 3D surface models from medical images. Generation of a surface model from the 2D contour data began with the translation of the segmented, modified, and smoothed contour points into a data series that was loaded into ANSYS preprocessing software packages GAMBIT and TGrid. GAMBIT and TGrid were used to modify the surface mesh and then create a volume mesh of the model, respectively. Surface geometries of respiratory tract were also exported as STL format. Fig. 2 shows two views of the human airway model after going through

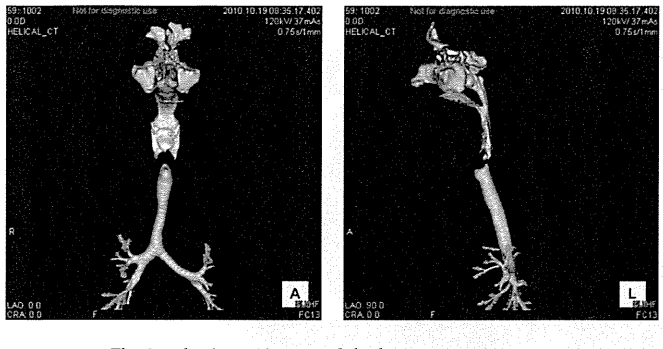

Fig. 1. Selective CT images of the human upper airways.

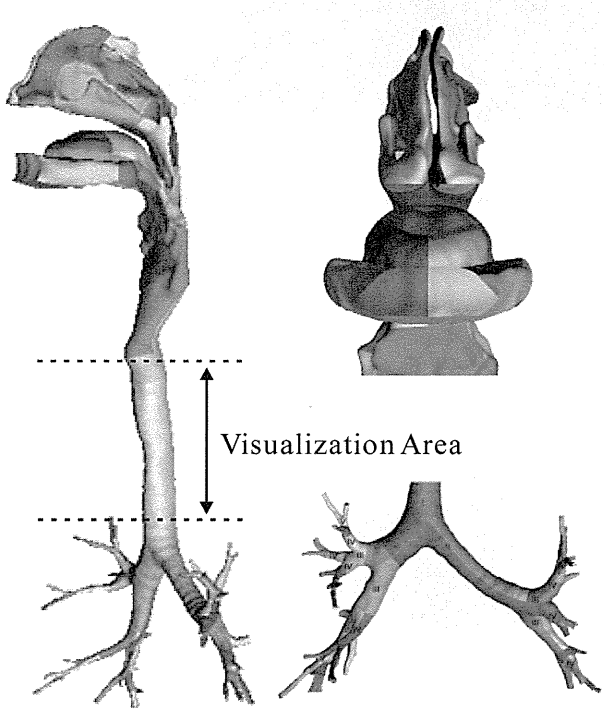

Fig. 2. A schematic of the human airway model.

this process. This respiratory tract model is composed of an upper airway (nasal and oral cavity, Pharynx and larynx) and lower airway (trachea and bronchial tree), as described in Fig. 3(a). The respiratory tract model possessed the height and volume of about 34.8 cm and 173 cm^3, respectively.

Using the STL data, a three-dimensional respiratory tract model was created with a 3D printer (Objet Connex 500). The lamination layer (Z direction) was 16 μm and the object resolution was 600 dpi (x) × 600 dpi (y) × 1600 dpi (z). The respiratory tract model was created with a transparent acrylic material (Objet Vero Clear RGD 810). As described further below, the mesh resolution of CFD simulation is on the order of 0.01–0.1 mm (10–100 μm). This CFD mesh resolution is in the same range as the 3D-printed model. The respiratory tract model in the 3D printer is shown in Fig. 3(b).

3.2. The experimental setup of PIV

PIV is a technique that measures the instantaneous velocity field within an illuminated plane of the fluid field using light scattered from tracer particles in the fluid. The particle locations are determined by capturing the scattered light from the individual particles with a digital camera. The particle displacement in the region of interest is calculated by comparing consecutive images. A two-dimensional map of the two-component velocity vectors is then derived by dividing the displacement distance by the known time delay between the images. The analysis of the PIV images is conducted by dividing the image into a grid of smaller sub-areas called interrogation areas. A displacement vector for the tracer particles is then detected in each interrogation area by using the cross-correlation statistical method. This process is repeated for the next interrogation area until all areas are complete. Then the calculated results could be shown in the velocity vector map.

In the PIV measurement of this study, a two-dimensional flow field was measured using hollow glass spheres (60 μm) as tracers for visualization. The high-speed Photron FASTCAM APX camera recording on a complementary metal-oxide-semiconductor (CMOS) sensor was used to capture the particle motions. Two experimental parameters that are important for accurate results of measuring the particle movement are the illumination power and the delay time between images. A continuous wave (CW) laser (Beamtech Optronics, diode-pumped solid state (DPSS) green laser, 2 W, 532-nm wavelength) was used as a light source. The field of view of the CMOS camera could resolve a region of 32 mm × 64 mm by illuminating a light sheet of 3-mm nominal thickness discharged from the laser. The frame rate was defined as 500 fps with a resolution of 512 × 1024 pixels. The PIV measurement apparatus is shown in Fig. 4. For the current research, images were divided into interrogation windows of 16 × 16 pixels with 50% overlap. Single exposed image pairs were analyzed, which are single exposure/single frames analyzed by means of adaptive correlation. The image data were analyzed using the Dynamic studio software package Dantec Dynamics A/S. The vector fields were generated using cross-correlation fast Fourier transforms (FFTs) with an adaptive correlation based on Scarano and Riethmuller [43]. In the standard adaptive correlation, the two interrogation windows are discretely offset based on an estimate from the previous displacement estimates with the same or larger interrogation regions. The vector field was filtered for spurious vectors using velocity range, peak ratio, and local median filters. The mean flow properties were then obtained by taking an ensemble average of the instantaneous velocity vector maps. A map of the statistical velocity vectors was made using the averaged velocity vector field of the trachea plane calculated from 4000 PIV images. Fig. 3(b) shows the experimental setup with the suspended airway model and with pipework for the PIV system.

For the current application, a mixture of water and sodium polytungstate was used as a working fluid to match the refractive index (*RI*) of the flow (working fluid) and acrylic material constituting the airway model. The refractive index also dictates the relationship between the working fluid and the model material in order to eliminate the refraction of the laser sheet. The refractive index of the acrylic used for model construction is specified as 1.51. To duplicate actual breathing conditions, the fluid should have the same Reynolds number (Re) in both the numerical simulations and the experimental measurements. The relationship is given as follows:

$$Q_{mixture} = \frac{\nu_{mixture}}{\nu_{air}} Q_{air} \tag{1}$$

where $Q_{mixture}$ is the volumetric flow rate and ν is the kinematic viscosity. The kinematic viscosity of the working fluid is $\nu = 1.747 \times 10^{-6}$ m^2/s, as determined using Cannon-Fenske Routine Viscometers. The density is $\rho = 2.47 \times 10^3$ kg/m^3 at the temperature maintained during the experiments (25 °C).

The flow rate at which the flow changes from a laminar to a

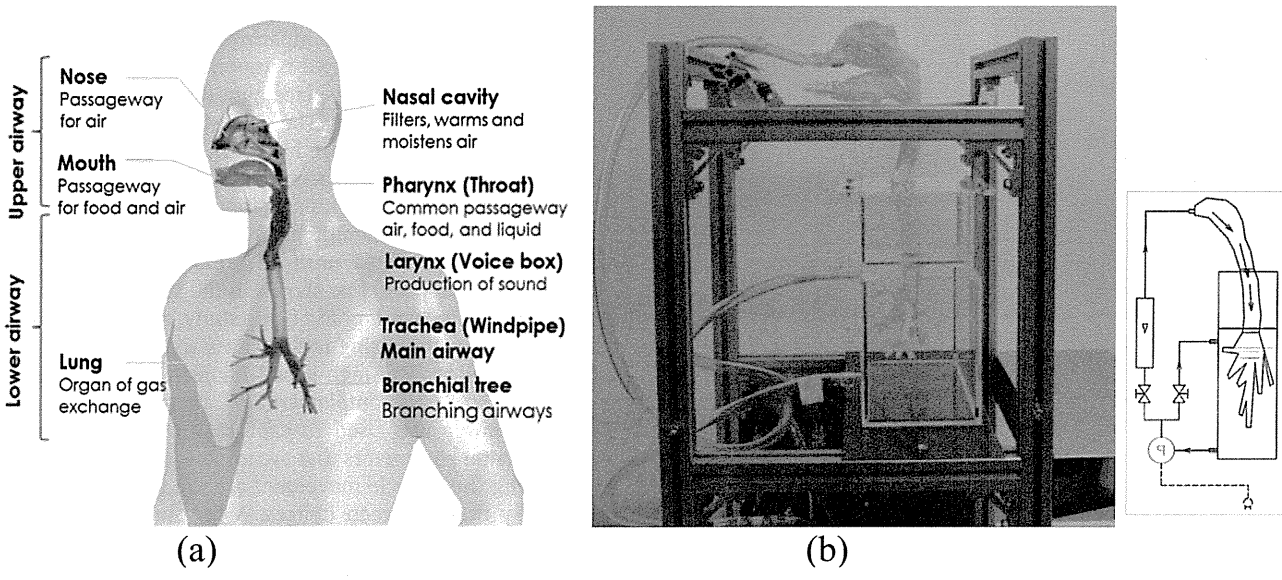

Fig. 3. A computational human airway model with labels (a), and an acrylic human airway model made by 3D printer and experimental set up (b).

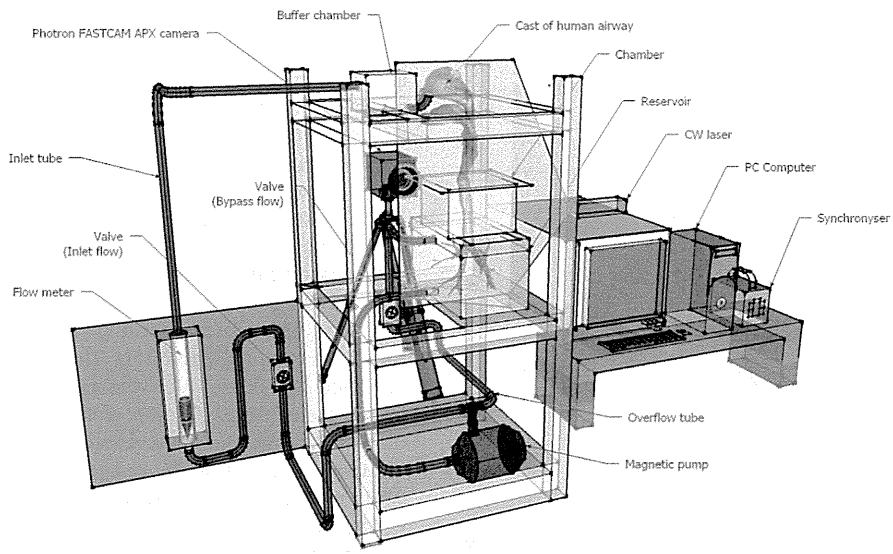

Fig. 4. Sketch of the experimental PIV apparatus.

turbulent flow regime has uncertainty because of the complexity of the geometry. Kelly et al. [25] conducted experimental studies that suggested that laminar flow remains at low flow rates near 10 L/min. Recent numerical simulations of realistic nasal airways show a consensus among researchers in using a laminar flow for flow rates less than 20 L/min [38,44]. In the current research, the Reynolds numbers for steady flow measurement were approximately 500 for the 7.5 L/min air flow rate, 1000 for the 15 L/min air flow rate, and 2000 for the 30 L/min air flow rate for the different flow rates. Two types of inhalation condition were assumed: nasal inhalation and oral inhalation.

The trachea region of the airway model was immersed in the working fluid (the mixture of water and sodium polytungstate) and suspended in the rectangular Plexiglass box. The outlet of the model was connected to the lower reservoir. The working fluid was pumped from the reservoir to the inlet opening of the model. An overflow tube was also connected to guarantee a constant level in the reservoir. The flow rate was regulated by a flow control valve that was placed behind the high-pressure flow meter (Kofloc model RK1400 with accuracy of ±2%). The PIV measurements were obtained for a two-dimensional flow field using hollow glass spheres (60 μm) as tracers for visualization.

Fig. 4 provides a sketch of the full experimental set up for PIV measurements. Fig. 5(a) shows the appearance of PIV measurements with visualization by laser light sheet. Fig. 5(b) is a photograph of the trachea region immersed in the sodium polytungstate/water mixture with a matching refracting index. Fig. 5(c) shows six cross-sectional slices along the trachea region. The three-dimensional geometry of the bronchial air pathway used in the realistic respiratory tract model is also shown in Fig. 5(c).

3.3. *Creation of numerical airway model and CFD simulation*

CFD simulations were performed to calculate airflow profiles

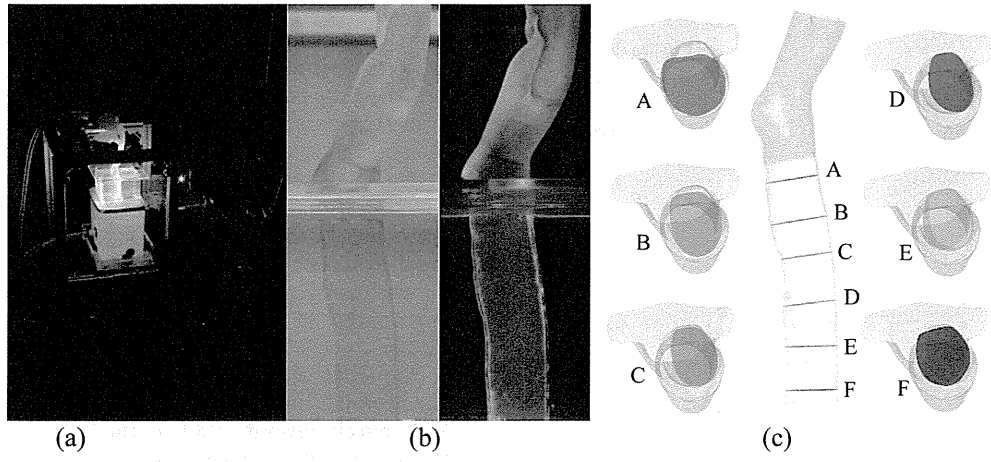

Fig. 5. Appearance of PIV measurement with laser and camera (a), photograph depicting trachea region immersed in sodium polytungstate/water mixture matching the refracting index (b), and six cross-sectional slices along the trachea region (c).

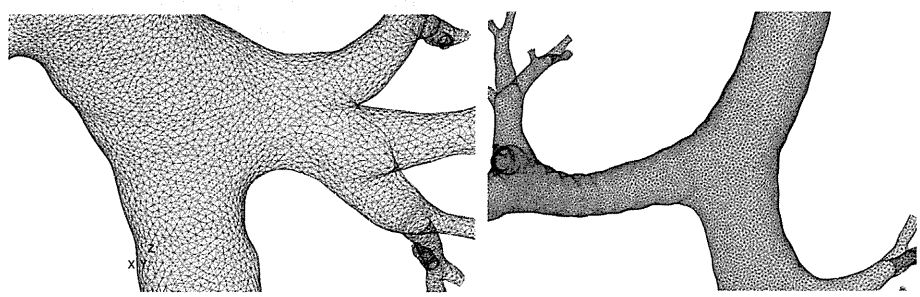

Fig. 6. Representative grid design of numerical airway model.

under three breathing conditions. Steady flow fields were analyzed using low Reynolds number k–ε by Abe et al. [45] and Launder-Sharma model [46], a renormalization group (RNG) k–ε model by Yakhot and Orszag [47], and a shear-stress transport (SST) k–ω model by Menter [48].

The low-Re k–ε models were designed to account for damping and echo effects in the near wall region. It is also applied to quasi-laminar flow fields existing within stable stratifications. The model implements damping and model functions, and performs low-Reynolds number corrections for the production and dissipation terms of the eddy viscosity μ_t and ε equations. The low-Re k–ε models are established method to simulate turbulence phenomena found near walls in the refined mesh layers in the region near a wall with no-slip conditions. The analyses performed in this study use the Abe- Nagano - Kondoh model (LR-ANK) and Launder-Sharma model (LR-LS).

The RNG k–ε model applies the Re-Normalization Group (RNG) theory and is similar to the standard k–ε model (although numerical constants such as C_μ and $C_{\varepsilon 1}$ differ). It has a built-in low-Reynolds number effect that is used to calculate Prandtl numbers found in the diffusion terms of transport equations for k and ε in regions with high Reynolds numbers. This occurs in the appearance of additive terms that reproduce distortion effects found in the ε transport equations.

The SST k–ω model is a hybrid model of the k–ω model for boundary layers around wall surfaces and the standard k–ε model used outside of boundary layers. In the k–ω model, there is no need to use damping functions in viscous sublayers because low-

Table 1
Numerical and boundary conditions.

Turbulence model	Low Re type k–ε model (Abe- Kondoh- Nagano model) RNG k–ε model SST k–ω model
Mesh design	7.5 million cell mesh (Unstructured, Tetrahedral)
Algorithm	Steady state with SIMPLE algorithm
Scheme	Convection term: QUICK Others: second order center difference
Inflow boundary	U_{in} = 0.475 m/s (nasal inhalation), =0.326 m/s (oral inhalation) (7.5 L/min) U_{in} = 0.950 m/s (nasal inhalation), =0.652 m/s (oral inhalation) (15 L/min) U_{in} = 1.900 m/s (nasal inhalation), =1.303 m/s (oral inhalation) (30 L/min), TI = 10%, k_{in} = 3/2 $(U_{in} \times 0.1)^2$, $\varepsilon_{in} = C_\mu^{3/4} k_{in}^{3/2} l_{in}$,
Outflow boundary	U_{out} = Free slip, k_{out} = Free slip, ε_{out} = Free slip
Wall treatment	Velocity: no slip
Others	Isothermal condition

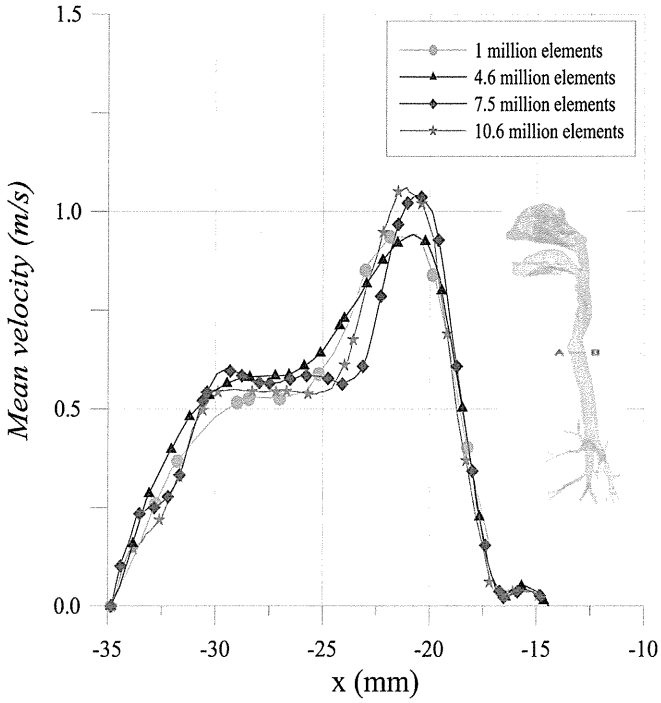

Fig. 7. The results of the grid dependence check.

Reynolds number corrections have been made in the coefficient of eddy viscosity, μ_t.. The value of turbulent kinetic energy at the inlet, i.e. at the nostril, was prescribed assuming a turbulence intensity of 10%. A no-slip boundary condition was applied for the wall surfaces inside the airway model. The second-order upwind scheme was used for the convection term, and the SIMPLE algorithm was used.

The geometric shape of the surface was constructed using a tetrahedral mesh. Representative grids of the numerical airway model are shown in Fig. 6. The first mesh wall surface is set within the viscous sub-layer and the wall units (y^+), which express the dimensionless normal distance from the surface, satisfying the requirement of 1.0 or less over the whole surface of the airway model.

Numerical and boundary conditions are summarized in Table 1. The Reynolds number, based on the inlet, had values of 500 for the 7.5 L/min air flow rate, 1000 for the 15 L/min air flow rate, and 2000 for the 30 L/min air flow rate in accordance with experimental conditions. In the case of nasal inhalation, average inlet velocities were set to 0.475 m/s (7.5 L/min), 0.950 m/s (15 L/min) and 1.900 m/s (30 L/min). The areas of nasal inlet were 0.0001288 m^2 (left) and 0.0001329 m^2 (right). For oral inhalation, the average inlet velocities were set to 0.326 m/s (7.5 L/min), 0.652 m/s (15 L/min), and 1.303 m/s (30 L/min). Isothermal conditions were assumed in accordance with experimental scenarios.

3.4. Creation of simple computational and replica model

Prior to the PIV experiment with a realistic and complicated replica human model, the PIV measurements on a simple model

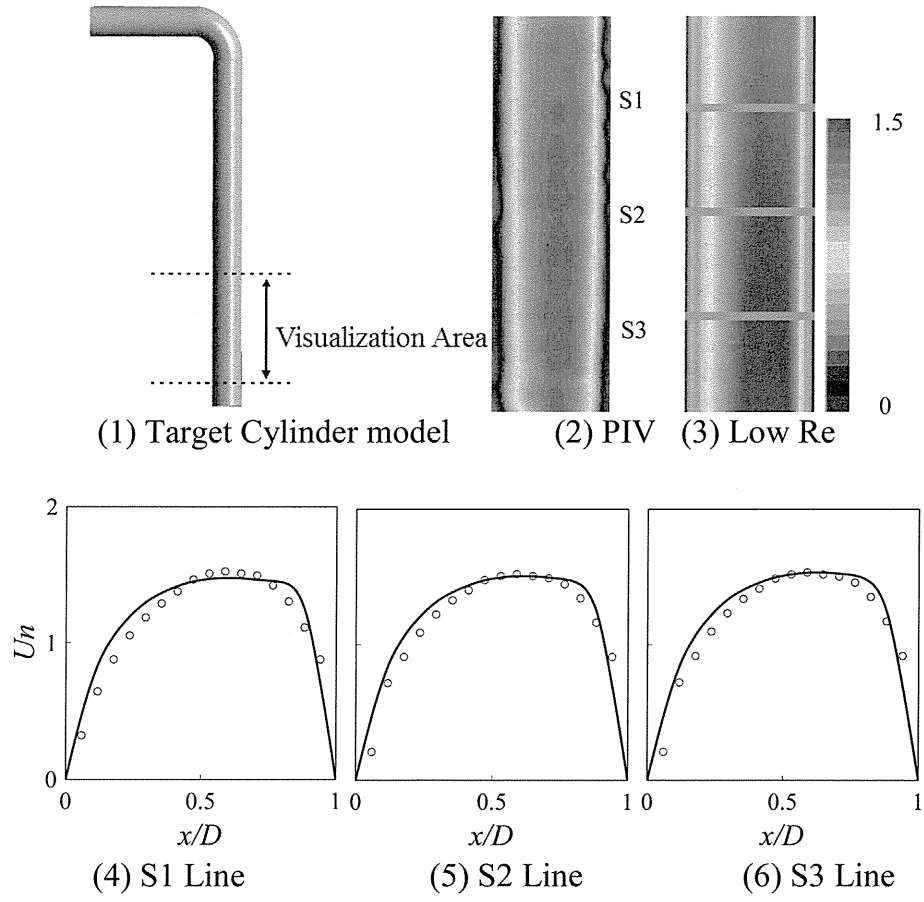

Fig. 8. Flow Pattern in Idealized Cylindrical model by PIV and CFD (Red circle: PIV, Black line: Low Re k–ε ($U_n = U/U_{in}$, $U = \sqrt{U_x^2 + U_y^2}$). (For interpretation of the references to colour in this figure legend, the reader is referred to the web version of this article.)

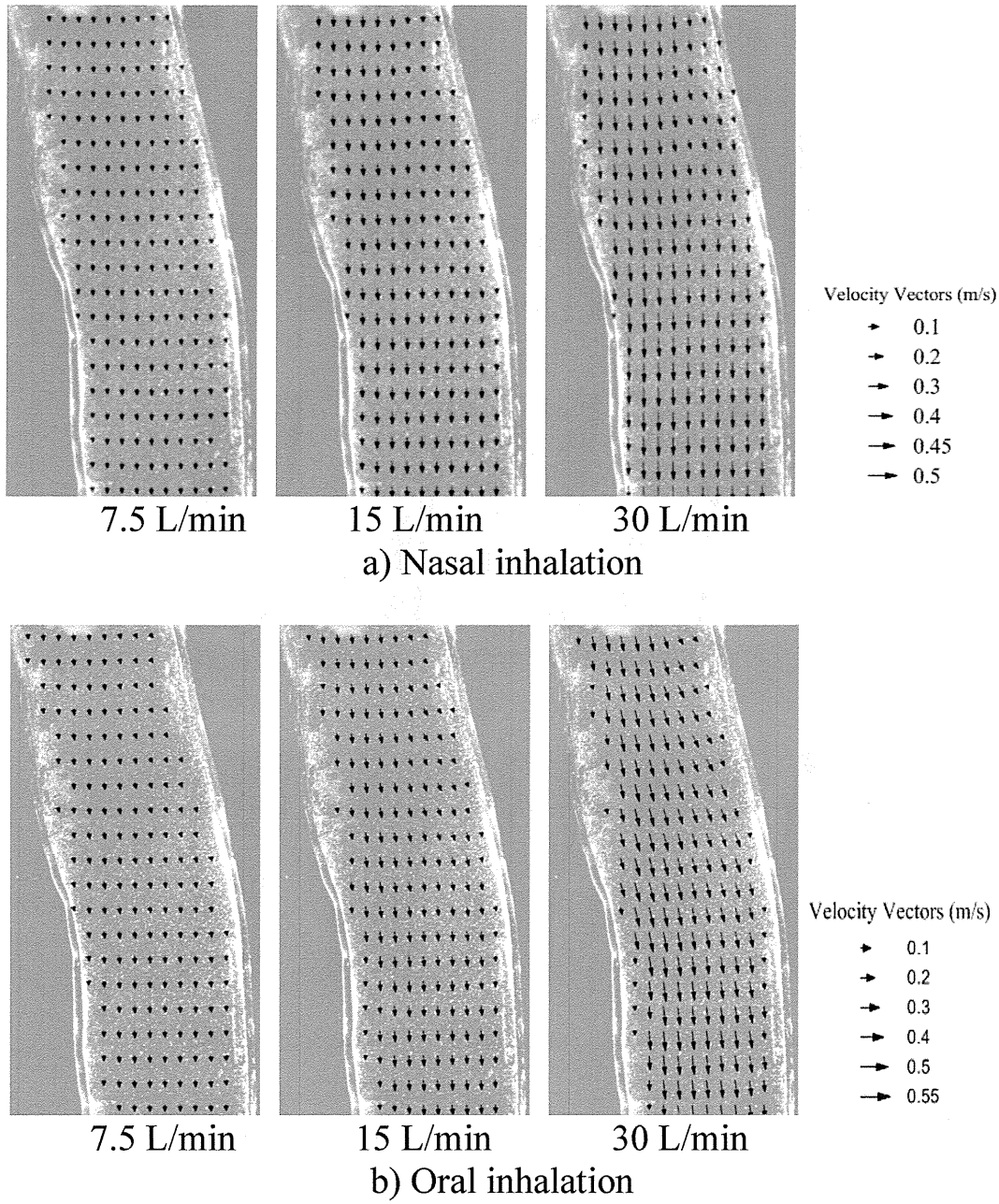

Fig. 9. Plots of two dimensional mean velocity vectors in central sagittal plane of nasal inhalation (a) and oral inhalation (b).

with a 90° bend were conducted. The model was constructed in three dimensions in accordance with the realistic human airway geometry as described above. With regard to a convoluted pathway such as the human respiratory system, it is quite difficult to designate an idealized geometry to represent the entire domain of the airway. Therefore, the characteristic dimension of the trachea was considered representative of that in the realistic geometry. To create the simple geometry, the primary features of the realistic airway model were examined at 10 cross slices of the trachea by ICEM CFD software (ANSYS, Inc.). The diameters of each slices were identified and averaged, and then, they were adopted as a reference to create a parametric model. The simple cylindrical model took shape based on the realistic shape and had diameter of 2 cm. The simple model extending from the nostril entrance to the trachea was modeled in a straightforward manner, and the nasal cavity was also simplified to have a regular cross section. The cylindrical model consists of three parts: inlet pipe of 7–cm length, 90° bend section, and a straight outlet section of 23–cm length. Rapid prototyping (3D printer) was used to produce the idealized replica from the 3D computer model. A prototype idealized model was made from transparent acrylic material.

3.5. Grid dependence study

The adequacy of grid resolution is tested by verifying fluid result at the flow rate of 7.5 L/min. Fig. 7 shows CFD results of the grid dependence check with scalar velocities along the A-B section. Four levels of grid resolution were adopted: 1.0 million, 4.6 million, 7.5 million, and 10.6 million total mesh cells. The mean velocity taken at a cross-line at trachea region agrees well from case of 7.5 million

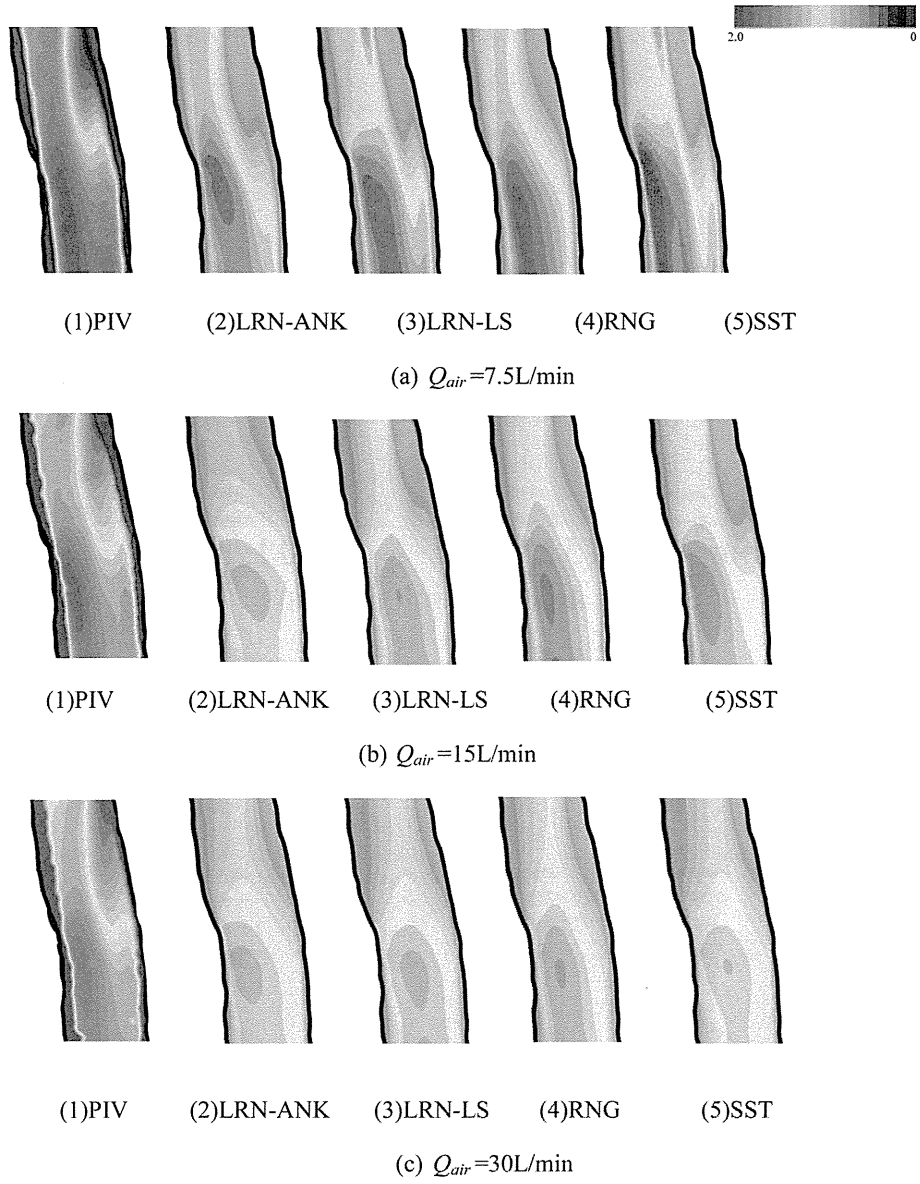

Fig. 10. Scalar Velocity Distributions by PIV and CFD under Nasal Breathing Condition.

meshes. Hence the human airway geometry in case of 7.5 million meshes is sufficient for predicting accuracy in this study.

4. Results

4.1. Idealized human airway model

The complexity of the physical model was also reduced with an idealized computational geometry. A corresponding CFD analysis with low Re type k–ε model (LR-ANK) was also conducted. The measurement and prediction results of the average air velocity magnitudes distributions by PIV and CFD are shown in Fig. 8. A relatively simple flow pattern was observed in both the PIV experiment and CFD prediction.

The mean velocities at cross line S1, S2, S3 in Fig. 8. (4), (5), (6) were normalized by inlet velocity which are indicated by the solid line in Fig. 8. (3). The CFD predictions were reasonably consistent with the results of PIV experimental data, and good agreement was observed. It was confirmed that flow profiles from CFD and PIV measurements was reasonably consistent with each other. Uniform steady flow at the model inlet was assumed. Despite this assumption, non-uniformity of the flow distribution between the inlet and outlet was demonstrated and confirmed.

4.2. Average fluid velocity distributions in airway by PIV

PIV measurement results of the average fluid velocity vector distributions are shown in Fig. 9.

Fig. 8 is the average velocity vector plots of nasal and oral inhalation respectively. The vector plots are quite similar for all three flow rates, indicating a similar flow structure across the range of flow rates. However, there are some minor structural variations with increasing fluid velocity that are worth noting. Fig. 9 reveals a notable phenomenon of flow inclination to the anterior side of the trachea. Because of the pressure gradient induced from centrifugal force, the secondary motion of the fluid persisted in the posterior side after the airflow passed around the bend from larynx (the upstream) to trachea (downstream) and hence flow separation

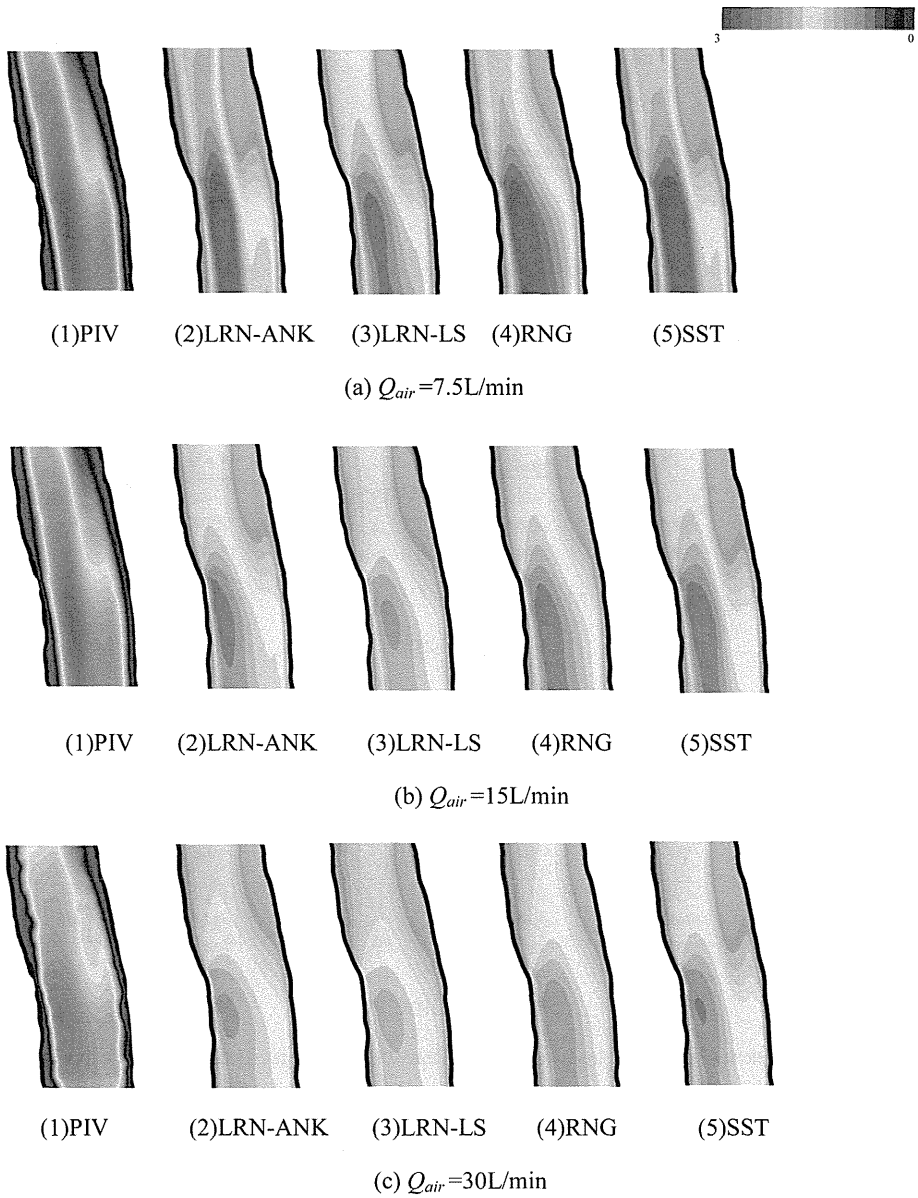

Fig. 11. Scalar Velocity Distributions by PIV and CFD under Oral Breathing Condition.

occurred with abrupt geometrical changes from the larynx to trachea. Further downstream in the trachea region, the flow fields become well developed. The laryngeal jet has a noticeable effect in the trachea region, as indicated by the more prominent velocity vectors on the left side of the images in Fig. 9. The primary effect of changing flow rates can be seen in Fig. 8a and b. Slight noise was caused by the surface reflection of the laser light sheet, especially at the upper and right-hand side of each figure. The velocity vectors have been scaled to a common reference value in order to improve the clarity of the results.

4.3. CFD analysis

4.3.1. Comparison with CFD simulation

CFD simulations were conducted to investigate the tracheal flow profile associated with the two inhaled modes (nasal and oral) and three flow rates. The three flow rates, Q_{air}, of 7.5, 15, and 30 L/min represent human activity conditions of rest, light work, and heavy work, respectively. CFD simulations were also conducted with the four different turbulent flow models discussed previously (two low Reynolds number type k–ε models (LR-ANK and LR-LS), an RNG type k–ε model, and an SST k–ω model). Figs. 10 and 11 are time-averaged velocity magnitude and PIV plots of these results for nasal and oral inhalation methods, respectively. CFD results can be compared with corresponding PIV maps. The velocity values were calculated as scalar velocities using two velocity components ($U_n = u_s/U_{in}$, $u_s = \sqrt{u^2 + v^2}$). In Fig. 10(a), the laryngeal jet is apparent, which transfers more momentum to the flow downstream (trachea). The flow is characterized by the region of separated flow at the start of the nasal/oral cavity, pharynx, larynx and down to trachea. The highest velocities in the flow field (>2 U_{inlet} and >3 U_{inlet}) are achieved at the left region in the trachea for nasal and oral inhalation. This acceleration is caused by an inclination, unique shape, and contracting cross-sectional area of the trachea region. Because of the "laryngeal jet," this high-speed flow enters the trachea at an angle, impinging against and flowing along the anterior wall of the trachea. This induces a recirculation region in the posterior half of the trachea which extends downstream

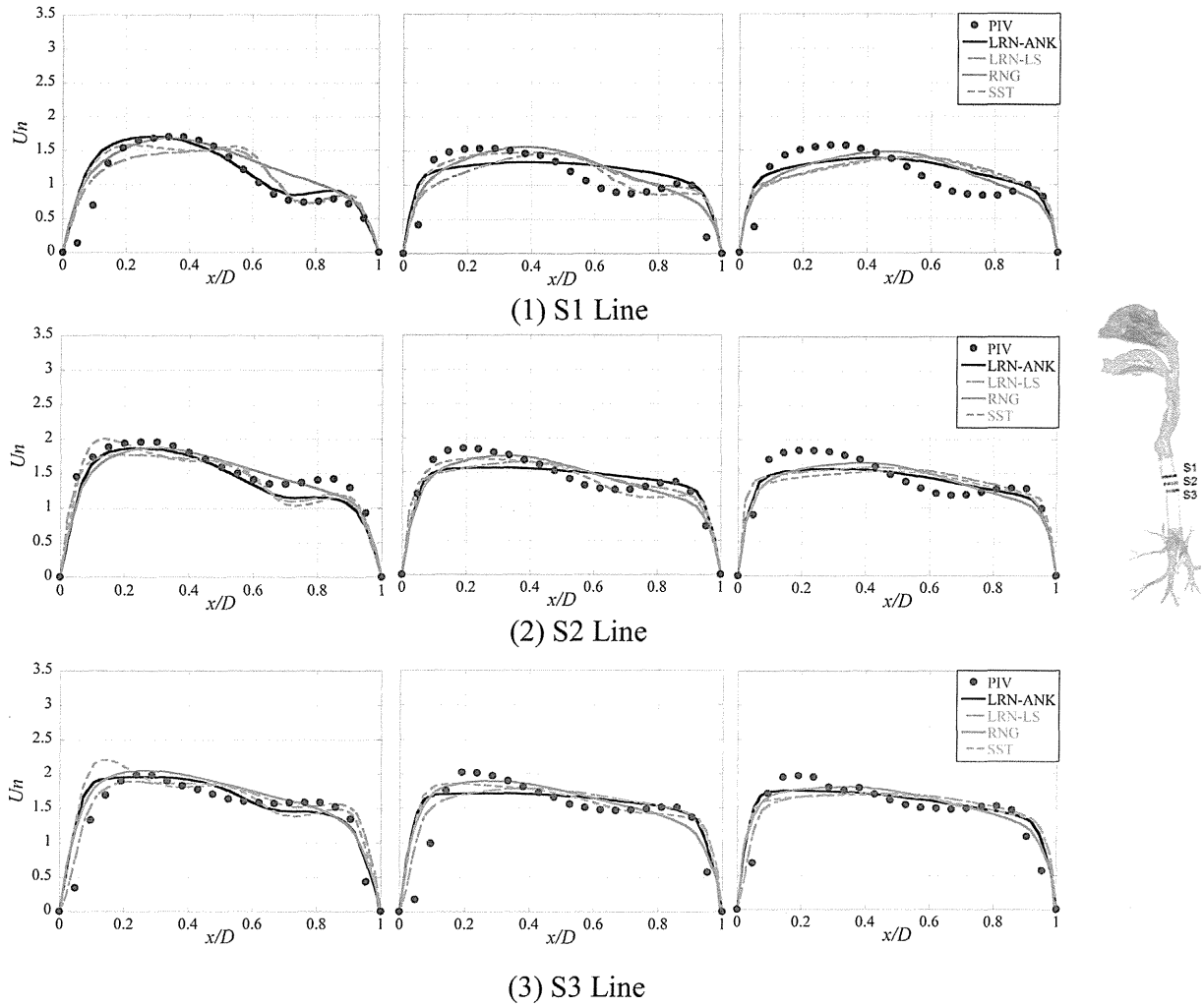

Fig. 12. Profiles of normalized scalar velocity under Nasal Breathing Condition (Left: 7.5 L/min, Center: 15 L/min, Right: 30 L/min) ($U_n = U/U_{in}$, $U = \sqrt{U_x^2 + U_y^2}$).

beyond the limit of measurements [28].

The velocity contours show that the basic structure of the flow field is predicted well by the CFD computations, and that changing the inlet boundary condition has some effect on the simulated flow structure. The effects of the different inlet conditions on velocity magnitudes are largely confined to the human airway via nasal/oral routes. The velocity magnitude plots for all three inlet conditions and both inhalation methods are reasonably similar to the experimental ones. All the major separation regions are well captured in the flow rates of 7.5 L/min and 15 L/min. The structure of the separated flow in the trachea is indicated in the CFD contour patterns.

In Figs. 12 and 13, the normalized velocity profiles for the three inspiratory flow rates are plotted at three cross section locations for nasal and oral inhalations, respectively. The distances of the cross sections at the PIV measurements and CFD predictions were made non-dimensional by dividing them by the diameter of trachea at that location. The starting point was defined as position x = 0 and the ending point was position x = 1 along the X-axis. The results in all cases show the fluid on the left hand (anterior) side moving faster while the fluid on the right hand (posterior) side is slower.

In Fig. 12, the CFD predictions for nasal breathing condition were reasonably consistent with the results of PIV experimental data, and good agreement was observed in the 7.5 L/min flow rate with two low Re number k–ε model. The turbulence model LR-ANK showed relatively better agreement compare to LR-LS at the peak velocity location. The air velocity profile trend in which air velocity becomes relatively high near the surface of the left side of trachea and air velocity gradually low at the opposite side (near to x = 1) was captured in all cross sections. The peak velocity for both of the experiment and the simulations were close to left wall.

The performance of the three turbulent models was also a subject of the current research. Using the SST k–ω model and RNG k–ε model did not match PIV measurements as well as with the low Reynolds k–ε models. The SST k–ω model in this study gave the poorest results from all the turbulence models. This model tended to over-estimate the airflow field due to an over-prediction of the effective viscosity, which can be clearly seen in sections S2 and S3 for the flow rate of 7.5 L/min. Results using the RNG k–ε model were not as good as the low Reynolds number k–ε model in matching PIV measurements because the velocity profile did not match the shape of PIV measured. The numerical simulation results tended to under-predict the velocities compared to the PIV measurement results in the cases of 15 and 30 L/min flow rates. The low Reynolds number k–ε model predictions were reasonably consistent with the results of PIV experimental data, and good agreement was observed in the case of Q = 7.5 L/min. The largest discrepancy occurred at the peak velocities, which was approximately 30%.

In Fig. 13, velocities in the CFD magnitude plots for the 7.5 L/min flow rate are much higher than the experimental results at three

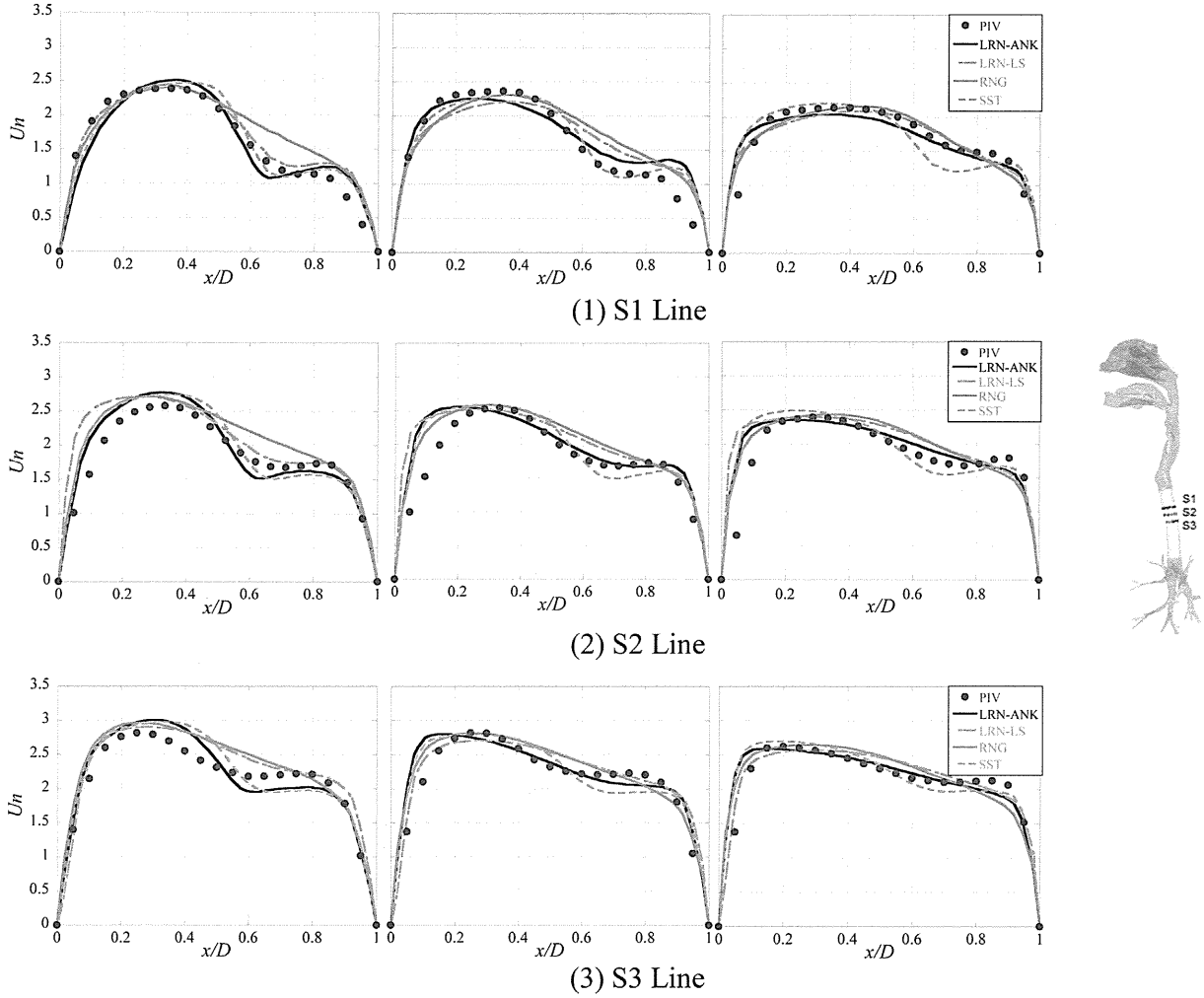

Fig. 13. Profiles of normalized scalar velocity under Oral Breathing Condition (Left: 7.5 L/min, Center: 15 L/min, Right: 30 L/min) ($U_n = U/U_{in}$, $U = \sqrt{U_x^2 + U_y^2}$).

cross sections. The velocities more closely match the experimental results for 15 and 30 L/min flow rates. It is notable that the velocity magnitude field changed appreciably with increasing flow rate. Comparing the trends from cross sections S1–S3, the velocity magnitudes increased as they progress further downstream. Zhang et al. stated that among the RANS models, RNG k–ε models have the best performance after performed various validating tests (in terms of accuracy, computing efficiency, and robustness) and recommended for indoor airflow simulations [49]. However, Phuong and Ito reported the RNG k–ε model performance was not good as LR-ANK turbulence model in predicting the airflow in a forced vertical duct because the lack of modification in predicting the near wall region [50]. In this study, the results of the LR-ANK k–ε turbulence model agreed better with experimental data than results with the LR-LS k–ε, RNG k–ε and SST k–ω turbulence models.

5. Discussion

In the PIV measurements, the total error in the estimation of a single displacement vector can be expressed as a sum of the bias error and the measurement uncertainty. Each displacement vector is associated with a certain degree of over- or under-estimation error, i.e., bias error, plus some degree of random error or measurement uncertainty. Bias errors include the correlation mapping error and the conversion error resulting from the conversion of the pixel spacing to dimensional measurements. These errors have been assumed to be negligible in this measurement. Measurement uncertainty resulted from the experimental data collection techniques. Common sources included variations and uncertainties in the particle image diameter, fluid flow rate, laser reflections, refractive index, and air bubbles stuck on the model surface.

Since the PIV results were used for validation, the experimental systems and methods were carefully checked to ensure that the experimental error was minimized. Therefore, it is assumed that discrepancies between the experimental and CFD results are errors with the CFD analyses. The flow field at the higher flow rate is very challenging for some turbulence models. In addition, the geometry is highly curved in many regions as it includes the nasal/oral cavity, pharynx, larynx and trachea. The flow pattern in the nasal cavity is used to complex flow due to its geometry. This can result in significant anisotropic turbulence, which is a limitation of the turbulence models used in this research.

6. Conclusions

We introduced a basic model that was not intended to reflect the exact behavior of the human airway but that incorporated sufficient geometrical characteristics to allow a realistic comparison. It should be noted that a rigid-wall model was developed and measured. The lack of cyclic wall motion in both experimental and

computational models is a significant limitation in the representation of air flows. This study provides additional contributions in validating the use of CFD analyses to understand and predict human airway flows. This paper aims to provide data with insight into the characteristic of flow pattern. Our results suggest that these airflows can be accurately predicted in complex models of the trachea region.

Acknowledgments

Dr. Shin-ichiro Aramaki (Kyushu University), Mr. Masato Yamashita (Kyushu University) and Mr. Kota Hirase (Kyushu University) provided valuable suggestions and support for the PIV measurements, for which the authors are deeply appreciative.

This project was partially supported by a Grant-in-Aid for Scientific Research (JSPS 21676005).

References

[1] WHO, World Health Statistics Report, World Health Organization, Geneva, 2008.
[2] D.W. Dockery, Epidemiologic evidence of cardiovascular effects of particulate air pollution, Environ. Health Perspect. 109 (2001) 483–486.
[3] R.D. Morris, Airborne particulates and hospital admissions for cardiovascular disease: a quantitative review of the evidence, Environ. Health Perspect. 109 (2001) 495–500.
[4] S. Murakami, S. Kato, J. Zeng, Flow and temperature fields around human body with various room air distribution, CFD study on computational thermal manikin (Part 1), ASHRAE Trans. 103 (1) (1997) 3–15.
[5] S. Murakami, S. Kato, J. Zeng, Numerical simulation of contaminant distribution around a modeled human body, CFD study on computational thermal manikin (Part 2), ASHRAE Trans. 104 (2) (1998).
[6] S. Murakami, S. Kato, J. Zeng, Combined simulation of airflow, radiation and moisture transport for heat release from a human body, Build. Environ. 35 (6) (2000) 489–500.
[7] D.N. Sorensen, L.K. Voigt, Modeling flow and heat transfer around a seated human body by computational fluid dynamics, Build. Environ. 38 (2004) 753–762.
[8] N.P. Gao, J.L. Niu, CFD study of the thermal environment around a human body, a review, Indoor Built Environ. 14 (2005) 5–16.
[9] N.P. Gao, J.P. Niu, H. Zhang, Coupling CFD and human body thermoregulation model for the assessment of personalized ventilation, HVAC&R Res. 12 (3) (2006) 497–518.
[10] N.P. Gao, H. Zhang, J.L. Niu, Investigating indoor air quality and thermal comfort using a numerical thermal manikin, Indoor Built Environ. 16 (1) (2007) 7–17.
[11] T. Hayashi, Y. Ishizu, S. Kato, S. Murakami, CFD analysis on characteristics of contaminated indoor air ventilation and its application in the evaluation of the effects of contaminant inhalation by a human occupant, Build. Environ. 37 (2002) 219–230.
[12] S. Zhu, S. Kato, S. Murakami, T. Hayashi, Study on inhalation region by means of CFD analysis and experiment, Build. Environ. 40 (10) (2005) 1329–1336.
[13] S. Murakami, Analysis and design of micro-climate around the human body with respiration by CFD, Indoor Air 14 (Suppl. 7) (2004) 144–156.
[14] K. Inthavong, Q.J. Ge, X.D. Li, J. Tu, Detailed predictions of particle aspiration affected by respiratory inhalation and airflow, Atmos. Environ. 62 (2012) 107–117.
[15] N.L. Phuong, K. Ito, Development of respiratory tract model for numerical simulation and analysis of convective heat transfer coefficient and particle deposition at inner surface of airway, Trans. SHASE Soc. of Heat. Air-conditioning Sanit. Eng. Jpn. 190 (2013) 31–39 (In Japanese).
[16] K. Ito, Integrated numerical approach of CFD and epidemiological model for multi-scale transmission analysis in indoor spaces, Indoor Built Environ. 23 (7) (2014) 1029–1049.
[17] T. Matsuo, S. Yoo, N.L. Phuong, K. Ito, Development of computer simulated person with numerical airway model, Part 1 analysis of breathing contaminant concentration and respiratory exposure: indoor air 2014, in: The 13th International Conference on Indoor Air Quality and Climate, Hong Kong, Paper ID: HP0532, 2014.
[18] S. Yoo, T. Matsuo, N.L. Phuong, K. Ito, Development of computer simulated person with numerical airway model, Part 2 improved thermo-regulation model with heat and moisture transfer detail analysis in respiratory tract: indoor air 2014, in: The 13th International Conference on Indoor Air Quality and Climate, Paper ID: HP0541, 2014.
[19] Y. Kadota, T. Matsuo, S. Yoo, N.L. Phuong, K. Ito, Development of computer simulated person with numerical airway model, Part 3 breathing air quality prediction by improved unsteady breathing flow model: indoor air 2014, in: The 13th International Conference on Indoor Air Quality and Climate, Paper ID: HP0732, 2014.
[20] P. Diodati, N. Paone, G.L. Rossi, E.P. Tomasini, Comparison of laser-doppler velocimetry, hotwire anemometry and particle image velocimetry for the investigation of a turbulent jet, SPIE 2052 (1993) 315–322. Laser Anemometry Advances and Applications.
[21] M. Sandberg, Whole-field measuring methods in ventilated rooms, HVAC&R Res. 13 (2007) 951–970.
[22] T. Kobayashi, M. Sandberg, H. Kotani, L. Claesson, Experimental investigation and CFD analysis of cross-ventilated flow through single room detached house model, Build. Environ. 45 (12) (2010) 2723–2734.
[23] M. Girardin, E. Bilcen, P. Arebour, Experimental study of velocity fields in a human nasal fossa by laser anemometry, Ann. Otol. Rhinol. Laryngol. 92 (1983) 231–236.
[24] S.K. Chung, S.K. Kim, Digital particle image velocimetry studies of nasal airflow, Respir. Physiol. Neurobiol. 163 (2008) 111–120.
[25] J.T. Kelly, A.K. Prasad, A.S. Wexler, Detailed flow patterns in the nasal cavity detailed flow patterns in the nasal cavity, J. Appl. Physiol. 89 (2000) 323–327.
[26] L.M. Hopkins, J.T. Kelly, A.K. Prasad, A.S. Wexler, Particle image velocimetry measurements in complex geometries, Exp. Fluids 29 (2000) 91–95.
[27] D. Doorly, D.J. Taylor, P. Franke, R.C. Schroter, Experimental investigation of nasal airflow, Proc. Inst. Mech. Eng. Part H J. Eng. Med. 222 (4) (2008) 439–453.
[28] A.F. Heenan, E. Matida, A. Pollard, W.H. Finlay, Experimental measurements and computational modeling of the flow field in an idealized human oropharynx, Exp. Fluids 35 (1) (2003) 70–84.
[29] Y.S. Cheng, Y. Zhou, B.T. Chen, Particle deposition in a cast of human oral airways, Aerosol Sci. Technol. 31 (4) (1999) 286–300.
[30] B. Grgic, W.H. Finlay, P.K.P. Burnell, A.F. Heenan, In vitro intersubject and intrasubject deposition measurements in realistic mouth–throat geometries, J. Aerosol Sci. 35 (2004) 1025–1040.
[31] T.R. Anthony, M.R. Flynn, A. Eisner, Evaluation of facial features on particle inhalation, Ann. Occup. Hyg. 49 (2005) 179–193.
[32] S.K. Kim, S.K. Chung, An investigation on airflow in disordered nasal cavity and its corrected models by tomographic PIV, Meas. Sci. Technol. 15 (2004) 1090–1096.
[33] S.K. Chung, S.K. Kim, Digital particle image velocimetry studies of nasal airflow, Respir. Physiol. Neurobiol. 163 (2008) 111–120.
[34] C.J.T. Spence, N.A. Buchmann, M.C. Jermy, S.M. Moore, Stereoscopic PIV measurements of flow in the nasal cavity with high flow therapy, Exp. Fluids 50 (2011) 1005–1017.
[35] C.J.T. Spence, N.A. Buchmann, M.C. Jermy, Unsteady flow in the nasal cavity with high flow therapy measured by stereoscopic PIV, Exp. Fluids 52 (2012) 569–579.
[36] J. Wen, K. Inthavong, J. Tu, S. Wang, Numerical simulations for detailed airflow dynamics in a human nasal cavity, Respir. Physiol. Neurobiol. 161 (2) (2008) 125–135.
[37] D. Elad, M. Wolf, T. Keck, Air-conditioning in the human nasal cavity, Respir. Physiol. Neurobiol. 163 (1–3) (2008) 121–127.
[38] S. Naftali, M. Rosenfeld, M. Wolf, D. Elad, The Air-conditioning capacity of the human nose, Ann. Biomed. Eng. 33 (4) (2005) 545–553.
[39] Z. Zhang, C. Kleinstreuer, Species heat and mass transfer in a human upper airway model, Int. J. Heat Mass Transf. 46 (25) (2003) 4755–4768.
[40] B. Ma, R. Vincent, C. Patricia, R. Theunissen, M. Riethmuller, C. Darquenne, CFD simulation and experimental validation of fluid flow and particle transport in a model of alveolated airways, J. Aerosol Sci. 40 (5) (2009), 403–141.
[41] Zhe Zhang, Clement Kleinstreuer, Computational analysis of airflow and nanoparticle deposition in a combined nasal–oral–tracheobronchial airway model, J. Aerosol Sci. 42 (3) (2011) 174–194.
[42] K.W. Stapleton, E. Guentsch, M.K. Hoskinson, W.H. Finlay, On the suitability of $K-\varepsilon$ turbulence modeling for aerosol deposition in the mouth and throat: a comparison with experiment, J. Aerosol Sci. 31 (6) (2000) 739–749.
[43] F. Scarano, M.L. Riethmuller, Iterative multigrid approach in PIV image processing with discrete window offset, Exp. Fluids 26 (1999) 513–523.
[44] G.J. Garcia, M.N. Bailie, D.A. Martins, J.S. Kimbell, Atrophic rhinitis: a CFD study of air conditioning in the nasal cavity, J. Appl. Physiol. 103 (2007) 1082–1092.
[45] K. Abe, T. Kondoh, Y. Nagano, A new turbulence model for predicting fluid flow and heat transfer in separating and reattaching flows-I. Flow field calculations, Int. J. Heat Mass Transf. 37 (1) (1994) 139–151.
[46] B.E. Launder, B.I. Sharma, Application of the energy dissipation model of turbulence to the calculation of flow near a spinning disc, Lett. Heat Mass Transf. 1 (2) (1974) 131–138.
[47] V. Yakhot, S.A. Orszag, Renormalization group analysis of turbulence. I. Basic theory, J. Sci. Comput. 1 (1986) 3–51.
[48] F.R. Menter, M. Kuntz, R. Langtry, Ten years of Industrial experience with the SST turbulence model, in: K. Hanjalic, Y. Nagano, M. Tummers (Eds.), Turbulence, Heat and Mass Transfer, vol. 4, 2003, pp. 625–632.
[49] Z. Zhang, W. Zhang, Z.J. Zhai, Q. Chen, Evaluation of various turbulence models in predicting airflow and turbulence in enclosed environments by CFD: Part 2—comparison with experimental data from literature, HVAC&R Res. 13 (6) (2007) 871–886.
[50] N.L. Phuong, K. Ito, Experimental and numerical study of airflow pattern and particle dispersion in vertical ventilation duct, J. Build. Environ. 59 (2013) 466–481.

Building and Environment 100 (2016) 172–185

Contents lists available at ScienceDirect

Building and Environment

journal homepage: www.elsevier.com/locate/buildenv

Prediction of convective heat transfer coefficient of human upper and lower airway surfaces in steady and unsteady breathing conditions

Nguyen Lu Phuong [a], Masato Yamashita [b], Sung-Jun Yoo [b], Kazuhide Ito [c, *]

[a] Faculty of Environment, Ho Chi Minh City - University of Natural Resources and Environment, 236B Le Van Sy Street, Ward 1, Tan Binh District, Ho Chi Minh City, Viet Nam

[b] Interdisciplinary Graduate School of Engineering Sciences, Kyushu University, 6-1 Kasuga-koen, Kasuga, Fukuoka, 816-8580, Japan

[c] Faculty of Engineering Sciences, Kyushu University, 6-1 Kasuga-koen, Kasuga, Fukuoka, 816-8580, Japan

ARTICLE INFO

Article history:
Received 20 December 2015
Received in revised form
12 February 2016
Accepted 21 February 2016
Available online 23 February 2016

Keywords:
Numerical airway model
Respiratory tract
Computational fluid dynamics
Convective heat transfer coefficient

ABSTRACT

Bio-effluent and metabolic heat production from the human body and its breathing activity can strongly influence the microclimate around the body. On the other hand, local properties of the microclimate around the human body can also significantly affect the interaction between the body and the surrounding environment by way of local flow and heat transfer characteristics close to the body. Breathing is one of the most essential activities in our lives, and the basic functions of breathing include exchanging gases (supplying oxygen from ambient air and removing carbon dioxide from the blood) and exchanging heat and moisture (sensible and latent heat). As a consequence, human beings experience lifelong interaction with indoor environments via inhalation. In this study, two types of three-dimensional respiratory tract models were developed using computed tomography data of a healthy human males. Computational fluid dynamics simulations are performed to analyze the airflow and temperature distributions inside respiratory tract models under various breathing conditions. We used low-Reynolds-number-type k-ε model to predict airflow in the airway models. The flow pattern inside the viscous sub-layer and convective heat flux on the airway tissue surfaces and convective heat transfer coefficients were analyzed. Through this study, the numerical errors were successfully identical, so this discrepancy of two airway models were assumed due to the differences in airway geometries and reflected individual specificity. Averaged and local convective heat transfer coefficient distributions of the human airway were summarized as functions of breathing airflow rate.

1. Introduction

Optimization of energy efficiency and pursuit of a clean and healthy environment are becoming more important issues in the field of sustainable building design [1,2]. Overall, uniform control of indoor environments is not efficient from the view point of energy savings [3–6]. Accordingly, the control objectives for indoor environments have been expanded from the macro-spaces of entire rooms to the micro-environments of local domains, such as the occupied zone, the space around the human body, the breathing zone, and the respiratory system [7,8].

In accordance with the expansion and elaboration of indoor environmental design techniques, the prediction accuracy and targets of numerical simulation tools have also become more precise in their demands [9–12]. Recently, commercial numerical simulation tools have been used widely, and an integrated numerical procedure using computational fluid dynamics (CFD) and a computer-simulated person (CSP) have been applied in indoor environmental design, especially for the design of personalized ventilation system, optimization of local thermal comfort, and so on [13–17]. With the accuracy advances of micro-environmental design around the human body, developing comprehensive human models has become expected along with improving prediction accuracy for the physiological and psychological reactions and the effects on the human body caused by non-uniform environments formed around the body.

In regard to skin surface temperature control resulting from interaction between indoor thermal environments and the human body, many research achievements have emerged along with the various thermoregulation models proposed [18–22]. Furthermore,

* Corresponding author.
E-mail address: ito@kyudai.jp (K. Ito).

http://dx.doi.org/10.1016/j.buildenv.2016.02.020
0360-1323/